UNIVERSITÄT DES SAARLANDES

McMaster University

Naturwissenschaftlich-Technische Fakultät
Fachrichtung - Physik
Arbeitsgruppe Dynamics of Fluids

Masterarbeit

The Molecular Structure of Human Red Blood Cell Membranes from Highly Oriented, Solid Supported Multi-Lamellar Membranes

eingereicht von

Sebastian Himbert, B.Sc.

geboren am 29.09.1990 in Püttlingen

verantwortliche Betreuer und Hochschullehrer

Prof. Dr. rer. nat. habil. Christian Wagner

Prof. Dr. rer. nat. habil. Maikel C. Rheinstädter

Saarbrücken, 29. Mai 2017

Contents

0. Introduction

There are various techniques that are used to study the interactions between drugs and cells. However, the interaction between a drug and the cell membrane - the barrier between inter- and intracellular medium - is difficult to determine and is the focus of current research. Various common drugs, such as aspirin and cortisone, have been shown to have a significant effect on the membrane structure [1, 2, 3, 4]. While those investigations study the interaction between drugs and artificial membranes, *i.e.* simple lipid bilayers, their impact on native cell membranes is challenging. Due to the complex structure of a cell membrane and the cell itself, it is difficult to separate cellullar lipid bilayers from other cell compartments and the cytoskeleton. This thesis presents a new protocol that allows to extract the membranes from red blood cells (RBCs) and to prepare highly ordered multi-lamellar stacks of these membranes on silicon wafers. The method and the data are published in [1]. Parts of this thesis are taken from this publication.

Human RBC ghosts were prepared by hemolysis. The name of these empty RBC vesicles originates from their appearance under the microscope. Although the original preparation protocol by Dodge, Mitchell and Hanahan [5] was a remarkable step in the development of membrane proteomics and lipidomics, modifications were necessary. The morphology of the vesicles, the hemoglobin concentration and the presence of the cytoskeleton were analyzed using fluorescence microscopy and Ultraviolet–visible (UV-vis) spectroscopy. Due to the observed complex structure and the present actin filaments, the ghost solution was sonicated before applied onto silicon wafers and slowly dried and annealed over several days. The vesicles fuse on the silicon substrate, resulting in highly ordered multi-lamellar stacks of RBC membranes.

X-ray diffraction was used to analyze the structure of these membranes. Multiple series of well developed Bragg peaks were observed indicating a high degree of orientation of the membranes. These series can be identified as signals from liquid ordered (l_o), liquid disordered (l_d) lipids and coiled-coils peptide domains. There

was evidence that the lipids form nanometer sized domains and the collected data allows to present a detailed picture of the domain- and membrane structure.
The RBC ghosts allows to analyze the effect of drugs on the structure of a native membrane. The effect of aspirin, which is one of the most common drugs from the class of non-steroidal anti-inflammatory drugs (NSAID's), was investigated. NSAID's are known to interact with cell membranes [4, 6, 7]. However, the data presented in this thesis indicates that aspirin incorporates preferably into the head group region of the liquid ordered lipid domains leading to a fluidification of these membrane domains [3].
Although the prepared samples were used to analyze the molecular structure of RBC membranes with X-ray diffraction, the presented preparation protocol may also be useful for various other experimental techniques, such as atomic force microscopy, electron microscopic techniques or related biophysical methods.
This thesis is divided into three parts. Chapters 1 and 2 present the theoretical and experimental background of the used methods and materials and important background knowledge about biomembranes in general and RBCs in particular. Chapter 3 introduces the developed preparation protocol whereas the structural analysis of RBC membranes and the discussion of the results can be found in Chapters 4 and 5.

1. Methods and Materials

X-ray and neutron scattering are common techniques that are widely used to determine the atomic structure of single molecules, such as proteins, and the composition of multimolecular structures, such as cell membranes. Various inelastic neutron scattering techniques can also be used to measure dynamic processes in soft matter.
In this thesis, X-ray diffraction was used to analyze the structure and composition of human red blood cell (RBC) membranes. The common drug Aspirin was used to study the effect of a drug on the membrane structure. The following paragraphs present a theoretical and experimental background of the used methods and materials.

1.1. Wide Angle X-Ray Diffraction

1.1.1. Theoretical Background

Scattering techniques are common in physical research. Laser-, electron-, neutron or X-ray scattering allow analyzing structures from about 10 pm up to μm scales. An overview of different scattering techniques and their resolution compared to biological and chemical dimensions is presented in Fig 1.1. In particular X-ray and neutron scattering are essential for biological research because they can resolve structures and dynamic beyond the resolution of optical microscopes. Compared to *Atomic Force Microscopy* (AFM), *Scanning Tunnel Microscopy* (STM) or electron microscopy, they have the additional advantage of a deeper penetration.
Since the theoretical description of the photoelectric effect by Albert Einstein [9] and the development of quantum mechanics, it is known that light can be modeled as a particle, as well as an electromagnetic wave. While the photoelectric effect can only be explained by supposing light to be a stream of particles, wave interference can only be clarified by Maxwell's wave model. In analogy to this wave-particle

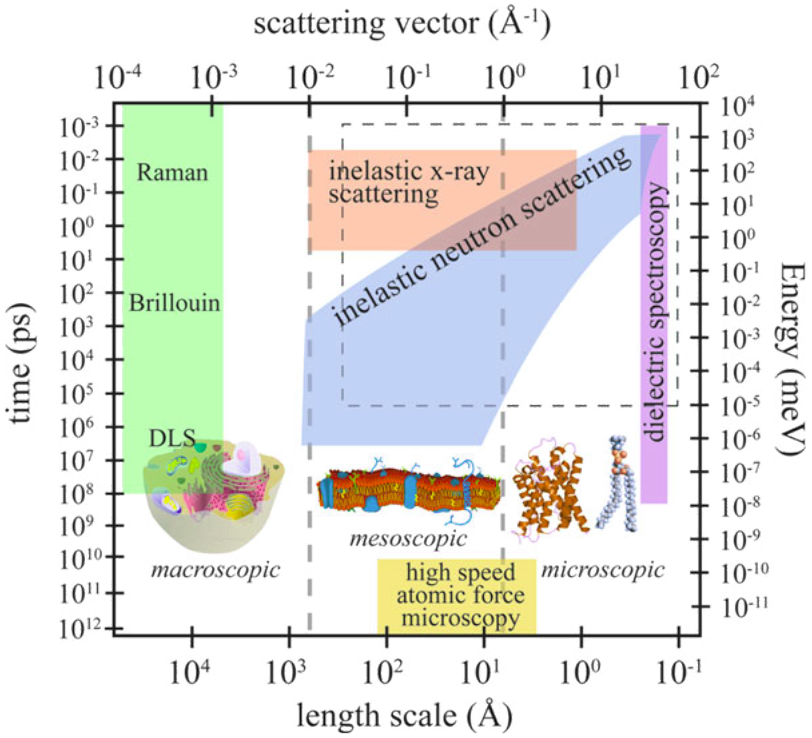

Figure 1.1.: The resolution of different scattering techniques compared to the dimensions of biological structures. While Raman, Brillouin and Dynamic Light Scattering (DLS) resolve structures in the size of cellular compartments, Neutron and X-ray Scattering are used to analyze structures such as biomembranes on a molecular scale. (Figure from [8])

duality of light, Louis de Broglie [10] proposed to describe massive particles also as waves. The wavelength of such a matter wave is defined by

$$\lambda_{dB} = \frac{h}{p}, \tag{1.1}$$

where h is the Planck constant and $p = |\vec{p}|$ is the absolute value of the momentum of the particles. Considering this relation, the main equations of the scattering theory can either be used for photons, neutrons or electrons.

Bragg's Law and Laue Equation

The structure of crystals was first analyzed by the pioneer in astronomy, Johannes Kepler, in his work *Strena seu de Nive Sexangula* [11], focusing on the crystals' regularity and symmetry. Due to the nonexistent experimental techniques, the first scientific investigation focused only on macroscopic structures like snowflake

crystals because it was not possible to determine the molecular or atomic structure. This research field experienced remarkable changes after the discovery of X-ray radiation by Wilhelm Conrad Röntgen in 1895 and the early work of Max von Laue [12, 13], William Henry Bragg and his son William Lawrence Bragg [14, 15] whose laid out the principles of X-ray diffraction. The theory and concepts of this technique can be found in various solid-state physics or crystallography textbooks. Unless otherwise stated, [16] is used primarily for the preparation of this thesis.

The idea of X-ray scattering is illustrated in Fig. 1.2 a). A crystal is modeled as a periodic array of atoms or molecules and X-Rays are considered to be electromagnetic waves. Two coherent beams approach the crystal under an angle θ and the waves get scattered on multiple layers of the crystal. The distance d between two layers results in a path difference between two reflected waves. Hence, these waves can interfere when the path difference, which is given by $2d\sin(\theta)$, is equal to an integer multiple of the wavelength. Hence, the condition for constructive interference is described by *Bragg's law*:

$$2d\sin(\theta) = n\lambda, \tag{1.2}$$

where n is the order of the interference peak, and λ is the wavelength. This equation allows determining the distance between two atomic layers by measuring the intensity of the reflected light versus the angle θ. In practice, it is common to use the scattering vector instead of the scattering angle, which describes the momentum transfer. This vector is defined as $\vec{q} = \vec{k}_f - \vec{k}_i$, where $\vec{k}_{i,f}$ are the incident and final (diffracted) wave vectors of the scattered X-rays (see Fig. 1.2 b)). The absolute value of this vector is related to the scattering angle and the distance d between two layers through:

$$\begin{aligned} |\vec{q}| &= \frac{4\pi\sin(\theta)}{\lambda} \text{ and} \\ |\vec{q}| &= \frac{2\pi}{d}. \end{aligned} \tag{1.3}$$

A crystal can be defined as an infinite sequence of identical structural elements [16] described by a lattice and a base (see Fig. 1.3), where the base is a single structural

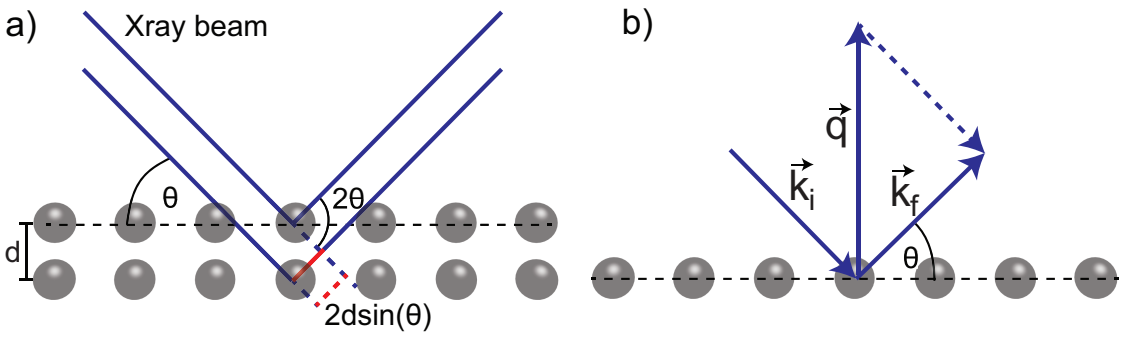

Figure 1.2.: a) Schematic illustration of Bragg's law. Coherent beams approach the crystal under an incident angle θ and get scattered by two layers. The scattered beams interfere constructively if the path difference of the scattered beams $2d\sin(\theta)$ is equal to an integer multiple of the wavelength. b) Schematic illustration of the scattering vector $\vec{q} = \vec{k}_f - \vec{k}_i$, where $\vec{k}_{i,f}$ is the incident and final (diffracted) wave vector of the scattered X-rays

---

element. The lattice is then a set of discrete translations in three-dimensional space

$$\vec{R} = n_1\vec{a}_1 + n_2\vec{a}_2 + n_3\vec{a}_3, \tag{1.4}$$

and is called the *Bravais lattice*. Here, the n_i are arbitrary integers, and the vectors $\vec{a}_i$, also called primitive vectors, span the lattice. The spanned cell is called the primitive cell and has the volume:

$$V_{ec} = \vec{a}_1 \cdot (\vec{a}_2 \times \vec{a}_3)\,. \tag{1.5}$$

A plane wave is defined by

$$\Psi(\vec{r}, t) = \Psi_0 e^{i\vec{k}\vec{r}} e^{-i\omega t} = \Psi_r(\vec{r})\Psi_t(t), \tag{1.6}$$

where Ψ_0 is the amplitude, $\vec{k}$ is the wave vector and $\vec{r}$ is the position vector. The corresponding reciprocal lattice is defined by the set of all wave vectors $\vec{k}$ with periodicity of the Bravais lattice, defined by Eq. 1.4. Hence,

$$\Psi_r(\vec{r}) = \Psi_r(\vec{r} + \vec{R}) = \Psi_0\left(e^{i\vec{k}\vec{r}} e^{i\vec{k}\vec{R}}\right). \tag{1.7}$$

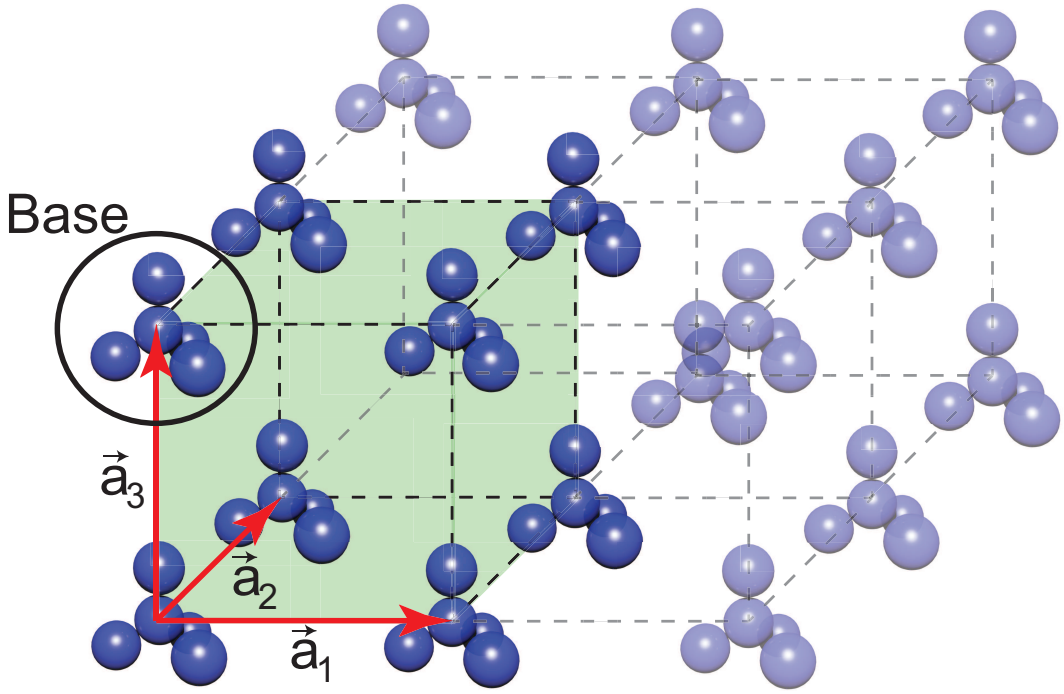

Figure 1.3.: Sketch of a Bravais lattice: An ideal crystal can be described as a lattice and a base, where the base is a single structural element (in blue) and the lattice is a set of discrete translations (see Eq. 1.4). The cell spanned by the vectors $\vec{a}_i$ is called the primitive cell (in green).

Therefore, the reciprocal lattice are all vectors $\vec{G}$ which fulfill:

$$\begin{aligned} e^{i\vec{G}\vec{R}} &= 1 \\ \Leftrightarrow \vec{G}\vec{R} &= 2\pi n, \end{aligned} \tag{1.8}$$

where n is an integer.
The vectors

$$\vec{G} = h\vec{b}_1 + k\vec{b}_2 + l\vec{b}_3 \tag{1.9}$$

with

$$\begin{aligned} \vec{b}_1 &= \frac{2\pi}{V_{ec}}\vec{a}_2 \times \vec{a}_3, \\ \vec{b}_2 &= \frac{2\pi}{V_{ec}}\vec{a}_3 \times \vec{a}_1, \\ \vec{b}_3 &= \frac{2\pi}{V_{ec}}\vec{a}_1 \times \vec{a}_2 \end{aligned} \tag{1.10}$$

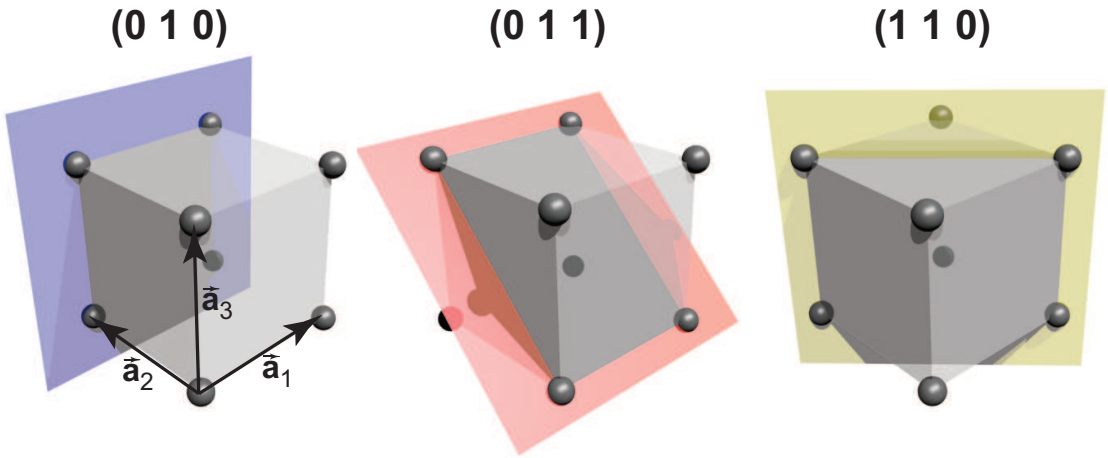

Figure 1.4.: Overview over different planes in an cubic lattice. Those planes are described by the Miller indices.

achieve this condition [16]. The integer coefficients h,k and l are known as the Miller indices and are related to the planes in crystal lattices, as described for instance in [16]. One can define such a plane by the intersections between the plane and the primitive vectors. The plane (hkl) intercepts the vectors $\vec{a}_{i=1\ldots3}$ at $(\vec{a}_1/h, \vec{a}_2/k, \vec{a}_3/l)$. Three examples of planes in a cubic crystal and the corresponding Miller indices are illustrated in Fig. 1.4.

Another description of scattering processes is given by Max von Laue [16]. An incident plane wave, given by Eq. 1.6, is incident on a Bravais lattice under the angle θ and spherical waves get emitted by every point of the lattice. The geometry is sketched in Fig. 1.5. Due to the distance between to points of the lattice, those coherent waves have a non-zero phase difference. The scattering is considered to be elastic, *i.e.* $|\vec{k}_i| = |\vec{k}_f|$. For constructive interference, the phase difference between two scattered waves needs to achieve the following condition:

$$|\vec{r}|\cos(\phi_f) - |\vec{r}|\cos(\phi_i) = n\lambda, \tag{1.11}$$

where n is an integer, λ is the wavelength of the incident beam and $\vec{r}$ is the euclidean vector between two scattering centers. One define the normal wave vectors:

$$\begin{aligned} \hat{\vec{k}}_i &= \frac{\vec{k}_i}{|\vec{k}_i|} = \frac{2\pi}{\lambda}\vec{k}_i \\ \hat{\vec{k}}_f &= \frac{\vec{k}_f}{|\vec{k}_f|} = \frac{2\pi}{\lambda}\vec{k}_f, \end{aligned} \tag{1.12}$$

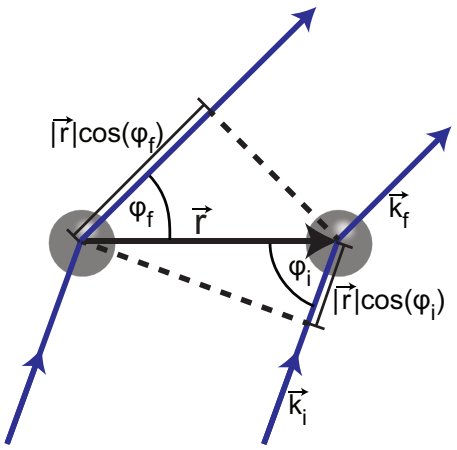

Figure 1.5.: Schematic illustration of a scattering experiment. The incident angle ϕ is related to θ from the Bragg condition over $\phi = 90-\theta$. The phase difference of two scattered beams can be calculated by $|\vec{r}|cos(\phi_f) - |\vec{r}|cos(\phi_i)$ and has to achieve Eq. 1.11.

and one can show that [16]

$$\begin{aligned} |\vec{r}|cos(\phi_i) &= \vec{r} \cdot \hat{\vec{k}}_i \\ |\vec{r}|cos(\phi_f) &= \vec{r} \cdot \hat{\vec{k}}_f. \end{aligned} \tag{1.13}$$

This results with 1.11 in:

$$\begin{aligned} \left(\hat{\vec{k}}_i - \hat{\vec{k}}_f\right) \cdot \vec{r} &= n\lambda \\ \Rightarrow \left(\vec{k}_i - \vec{k}_f\right) \cdot \vec{r} &= 2\pi n. \end{aligned} \tag{1.14}$$

Compared with 1.8, one gets

$$\vec{k}_i - \vec{k}_f = -\vec{q} = \vec{G}. \tag{1.15}$$

Hence, the spots of constructive interference in a diffraction experiment represent the lattice in the reciprocal space. Eq. 1.15 is also known as *Von-Laue equation*. The absolute value $|\vec{G}|$ is easily determined by using trigonometric relations. According to the geometry shown in Fig. 1.2 b), the absolute value is given by

$$|\vec{G}| = |\vec{q}| = 2k\sin(\Theta). \tag{1.16}$$

On the other hand:

$$|\vec{G}| = |\vec{q}| = \frac{2\pi}{d}. \tag{1.17}$$

By combining Eq. 1.16 and Eq. 1.17, and together with $k = \frac{2\pi}{\lambda}$, the Von-Laue

equation turns into Bragg's law.

Fourier Analysis

The intensity, which is observed in a diffraction experiment, can be calculated by [16]

$$I(\vec{q}) = |\Psi_r|^2 \propto \left| \int \rho(\vec{r}) e^{i\vec{q}\vec{r}} \mathrm{d}^3 r \right|^2 = |FT(\rho(\vec{r}))|^2 , \tag{1.18}$$

where $\Psi(\vec{r}, t)$ is the observed wave at point $\vec{r}$ and $\rho(\vec{r})$ is the scattering density, which is in case of X-rays equal to the electron density. If one could measure the complex amplitude Ψ_O, the electron density would be given by the inverse Fourier transformation of Ψ_O. However, the measurement of the intensity results in a loss of the phase information during the experiment [16].
By using the convolution theorem $FT(f * g) = FT(f) \cdot FT(g)$, the amplitude of the scattered wave can be written as

$$\psi_O = FT(g) \cdot FT(\rho_B), \tag{1.19}$$

where g is a lattice function, *i.e.* a superposition of delta peaks and ρ_B is the electron density of the base, *i.e.* a single molecule or atom. $S(\vec{q}) = FT(\rho_B(\vec{r}))$ is also known as the structure factor. We can apply the convolution theorem a second time and write ρ_B as a convolution of a new base function $b(\vec{r})$ and an atomic electron density ρ_A. The base function is, again, a superposition of delta peaks which describes the position of each atom. On the other hand, the function ρ_A is given by the electron density of a single atom. Because of the discrete structure of $b(\vec{r})$, the continuous integral in $S(\vec{q})$ turns into a summation over every atom:

$$\begin{aligned} S(\vec{q}) &= \sum_j f_j e^{i\vec{q}\vec{r}_j} \\ &\text{with} \\ f_j &= \int \rho_A(\vec{r}) e^{i\vec{q}\vec{r}} \mathrm{d}^3 r, \end{aligned} \tag{1.20}$$

where $\vec{r}_j$ is the position vector of the atom j and $\vec{r}$ is the radial position of an electron in the atom. The f_j are also known as the *atomic form factor*.
Although the described theory allows us to calculate the electron density from the X-ray diffraction data, limitations are apparent: While the scattering density is

determined by the form factor, the form factor itself depends on the scattering density.

This thesis focuses on the structure analysis of RBC membranes. The analysis of artificial single lipid bilayer structures by X-ray diffraction is a well established method in biophysical research [4, 17, 18, 19]. The data from the diffraction experiment were analyzed by a 1D Fourier analysis as sketched in Fig. 1.6. The intensity of the reflected beam as a function of q_z is given by [4, 17]:

$$R(q_z) = \frac{16\pi^2}{q_z^2} \left| FT(\rho(q_z)) \right|^2 . \tag{1.21}$$

As described above, the Fourier transformation of the electron density $\rho(q_z)$ is discrete due to of the lattice structure of a crystal. In the case of stacked lipid bilayers the grid function represents a lamellar structure. Hence the electron density can be calculated [20] by:

$$\begin{aligned} \rho(z) &= \rho_w + \frac{F(0)}{d_z} + \frac{2}{d_z} \sum_{n=1}^{N} F(q_n) \nu_n cos(q_n z) \\ &= \rho_w + \frac{F(0)}{d_z} + \frac{2}{d_z} \sum_{n=1}^{N} \sqrt{I_n q_n} \nu_n cos(q_n z). \end{aligned} \tag{1.22}$$

The bilayer form factor is, in general, a complex quantity. Assuming a centro symmetry, the form factor is real and given by $F(q_n) = \sqrt{I_n q_n}$ [21, 22], where I_n is the integrated peak intensity at position q_n. Further, the phase problem simplifies to a sign problem [4]: $F(q_n) = \pm |F(q_n)|$[4]. Hence, $\nu_n = \pm 1$ [4]. However, the phase information is lost during the experiment as described above. In order to determine the phases ν_n, a periodic function

$$\begin{aligned} T(q_z) &= \sum_{n=1}^{N} F(q_n) \mathrm{sinc}(\pi d_z q_z - \pi n) \\ &= \sum_{n=1}^{N} \sqrt{I_n q_n} \mathrm{sinc}(\pi d_z q_z - \pi n) \end{aligned} \tag{1.23}$$

can be fitted to the measured data $F(q_n)$ [1, 4, 21, 22]. $T(q_z)$ represents the discrete form factor, *i.e.* the electron density in Fourier space, of a single lipid bilayer. Once an analytic expression for $T(q_z)$ has been found, the phase factors ν_n can be determined from $T(q_z)$ [1].

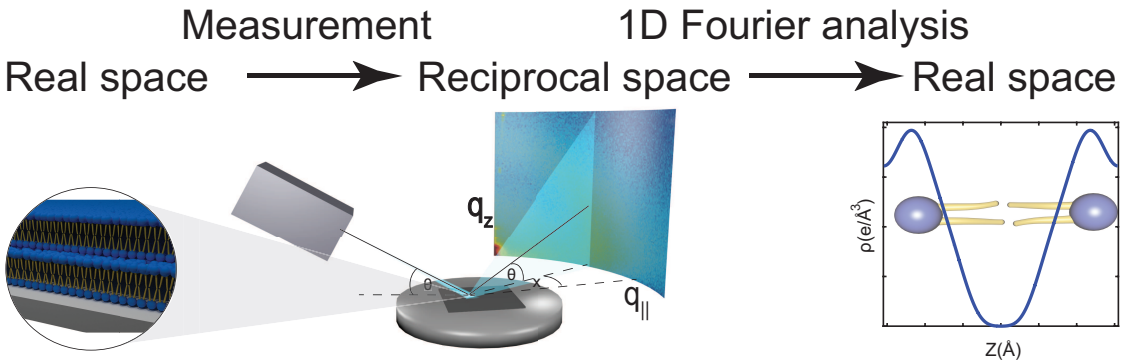

Figure 1.6.: The 2D X-ray intensity map, measured in an X-ray diffraction experiment is a representation of the structure in the reciprocal space. The scattering density in reals space, *i.e.* the electron density, can be calculated by a 1D Fourier analysis (see Eq. 1.22).

Scherrer's Equation

In a real X-ray diffraction experiment, the observed peaks are not delta-shaped. The broadening is on the one hand caused by the experimental setup and the precision of the measurement, but also caused by the size of the crystal. The described theory supposes infinitely expanded crystals, which is not feasible in an experiment. Furthermore, materials often show a poly-crystalline structure, *i.e.* they are composed of nanometer size monocrystals, also known as grains. Due to a diverse orientation, each monocrystal shows a different diffraction pattern. Paul Scherrer proposes in [23] a method to analyze the size of these monocrystals by measuring the broadening of the observed Bragg-peaks. Assuming a cubic lattice, the length L of a lateral edge of the cubic crystal is then given by

$$L = \frac{K\lambda}{B(2\Theta)\cos(\Theta)}, \tag{1.24}$$

where K is the Scherrer form factor, and $B(2\Theta)$ is the width of the first order peak in angle Θ in radians. The Scherrer form factor for a cubic Bravais lattice is $K = 0.94$. An overview of different Scherrer form factors for different lattices is given in [24].

1.1.2. Experimental Methods

The X-ray scattering data was obtained using the Biological Large Angle Diffraction Experiment (BLADE) in the Laboratory for Membrane and Protein Dynamics

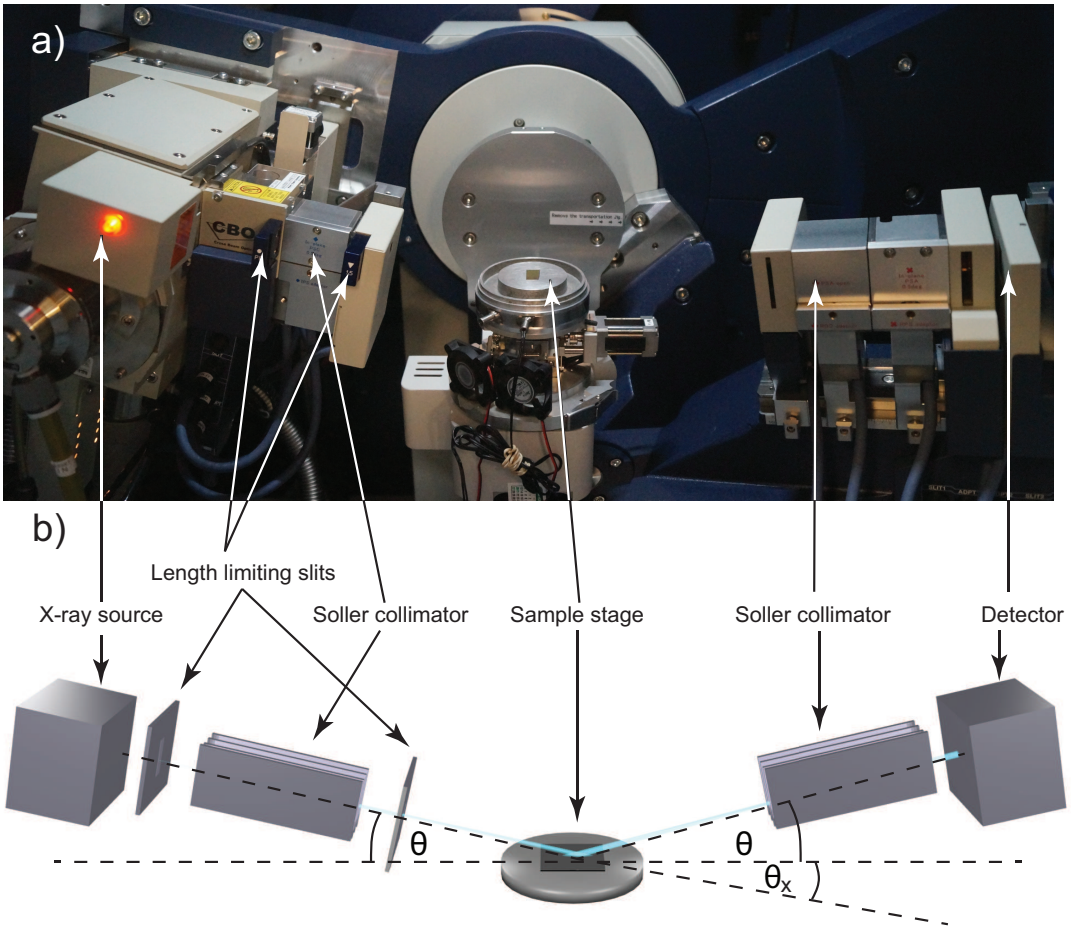

Figure 1.7.: Setup of the Biological Large Angle Diffraction Experiment (BLADE). The setup produces a wavelength of 1.5418 Å. Two soller collimators, and length limiting slits behind the X-ray tube and in front of the detector provide a high intensity parallel beam.

at McMaster University. BLADE is a SmartLab Intelligent X-ray diffractometer. It uses a 9 kW CuKα rotating anode with a maximum voltage of 45 kV and a maximum current of 200 mA. This setup produces a wavelength of 1.5418 Å. The optical setup is shown in Fig. 1.7. Both source and detector are mounted on movable arms such that the membranes stay horizontal during the measurements. This allows us the determination of the scattering vector.

Focusing multi-layer optics, based on length limiting slits and two soller collimators behind the X-ray tube and in front of the detector (see Fig. 1.7), provide a parallel beam with monochromatic X-ray intensities up to 10^{10} counts/(mm$^2\cdot$s). This beam geometry provides optimal illumination of the samples to maximize the scattering signal. Further, there is no risk of sample damage using this technique

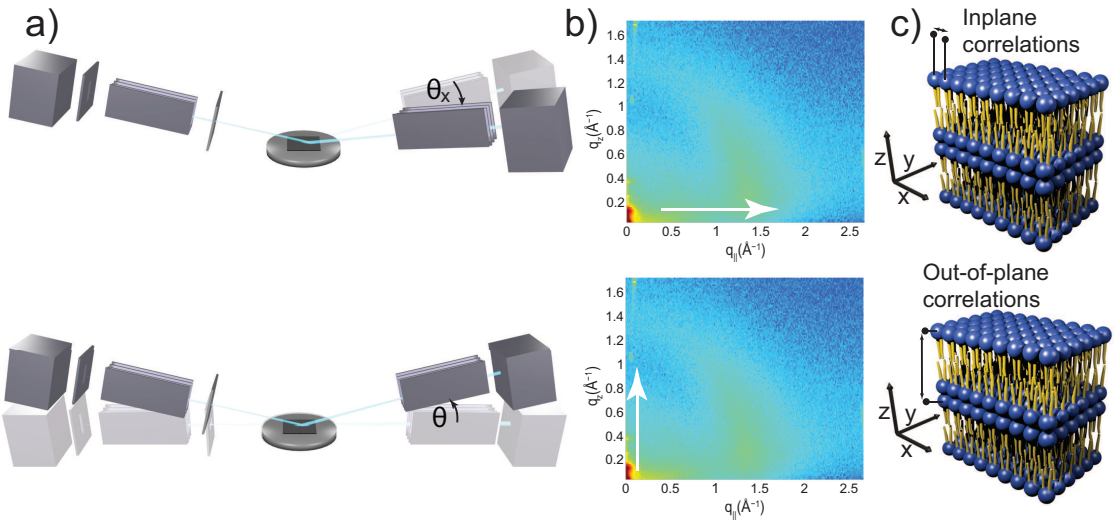

Figure 1.8.: a) During a measurement, BLADE varies the angle θ between 0° and ~12°. For each adjustment of θ, the angle θ_x is varied between 0° and ~18°. b) The result of an X-ray diffraction experiment is a 2D intensity map of the reciprocal space. c) Considering solid supported membranes, signals along the $q_{||}$-axis correspond to the distance between lipid tails [25] and signals along the q_z-axis correspond to the distance between two bilayers

because of the large beam size and relatively low intensity of the X-ray beam as compared to synchrotron sources. BLADE determines in-plane and out-of-plane structure separately, but simultaneously. The scanning path for a measurement is illustrated in Fig. 1.8 a) and b). The angle θ is varied typically between 0° and ~12°. For each adjustment of θ, the angle θ_x is varied between 0° and ~18°, resulting in a 2-dimensional intensity map of a large area of the reciprocal space, as sketched in Fig. 1.8 b). Signals along the $q_{||}$-axis provide information about structures parallel to the silicon substrate, signals along the q_z-axis provide information about structures perpendicular to the silicon substrate.
Considering solid supported membranes, those signals correspond to the distances between lipid tails ($q_{||}$) [25] and the distance between two bilayers (q_z) (see Fig. 1.8 c)), as described in the following paragraphs. A detailed analysis of the structure of solid supported RBC membranes is discussed in Chap. 4.

In-Plane Data Analysis

In order to calculate the overall scattered light from the in-plane structures, the 2D intensity map was integrated over a circular integration path. The resulting curve

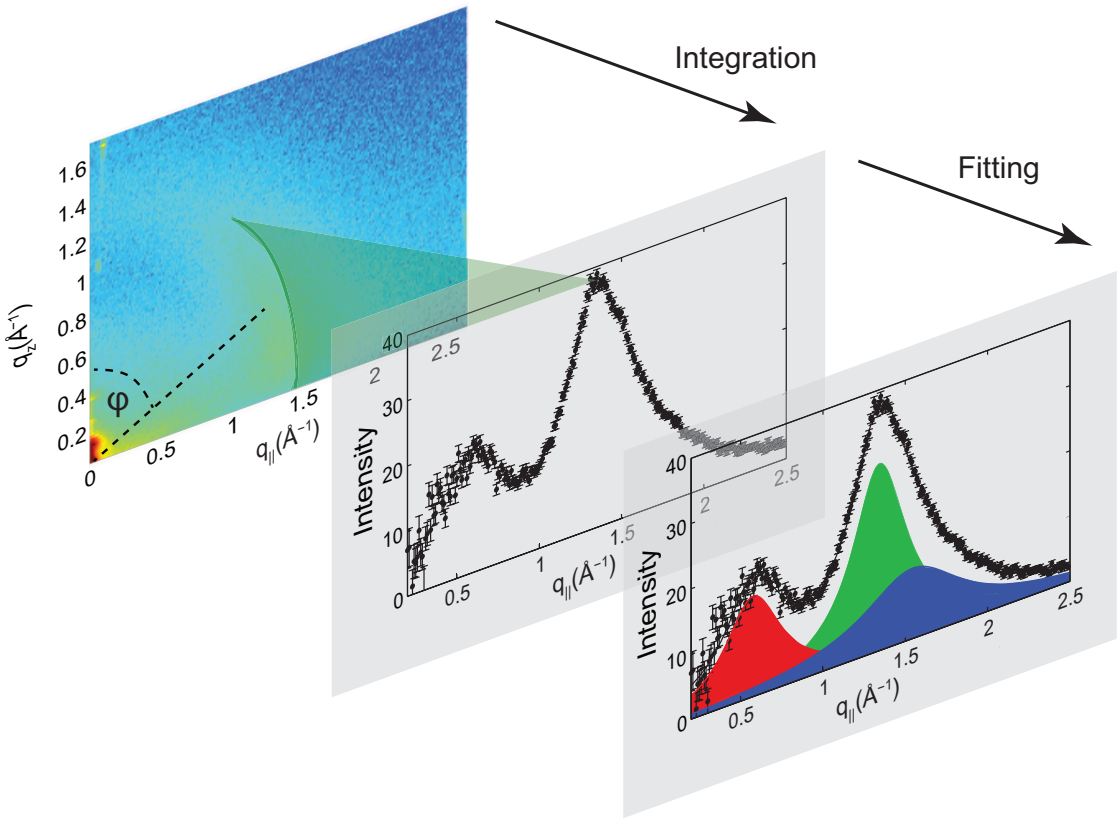

Figure 1.9.: Experimental data were analyzed by integrating the 2D intensity map over a circular integration path and fitting the resulting curve by a superposition of Lorentzian peaks.

was then fitted using a superposition of Lorentzian peaks as sketched in Fig. 1.9. Following Bragg's law, each peak corresponds to a correlation between molecular structures as described in Chap. 1.1.1. In case of lipid bilayers, the observed peaks originates from a hexagonal packing of the lipid tails in the hydrophobic membrane core (planar group p6) [25]. The distance between two lipid tails can be determined using

$$a = \frac{4\pi}{\sqrt{3}q_{||}}, \tag{1.25}$$

where $q_{||}$ is the peak position in Å^{-1}. Furthermore, the area per lipid tail can be calculated, using

$$A_T = \frac{\sqrt{3}}{2}a^2. \tag{1.26}$$

Scherrer's equation (Eq. 1.24) allows to estimate the domain size of the lipid patches found for RBC membranes (see Chap. 4). $K = 0.94$ was used as Scherrer form factor. While the Scherrer's equation is a well established way to estimate the crystallite sizes, the equation has limitations for smaller domains of a few nanometers. Further, the equation supposes cubic lattices, which disagree with the structures found for lipid bilayers. However, the quantity, calculated by Scherrer's equation, can be used as upper limit of the domain size [1].

Out-of-Plane Data Analysis

Previous investigations of single- and multi-component artificial lipid bilayer report well defined Bragg peaks along the q_z axis due to a high degree of orientation of the lipid molecules [26, 27, 28, 29, 30, 31]. Similar results were found for solid supported RBC membranes as discussed in Chap. 4. The observed Bragg peaks correspond to the 'fundamental' and 'overtones'. The data were fitted using a superposition of Gaussian peaks and the d-spacing, *i.e.* the distance between two bilayers were measured using $d = \frac{2\pi}{q_z}$ (see Eq. 1.3), where q_z is the position of the first order Bragg peak in Å^{-1}.
Multiple series of Bragg peaks were observed for the RBC membranes. The peak position was plotted *vs* the expected order of the Bragg peak in order to confirm a lamellar structure. Following Braggs law, the peak position goes linear with the order n. The electron density of all observed series of Bragg-peaks was calculated by a 1D Fourier analysis using Eq. 1.22. The phases were assigned by initial values. To verify the correct phases, the form factor $F(q)$ was calculated and fitted to the periodic function T_z (see Eq. 1.23) as described above [1].

Herman's Orientation Function

In order to determine the degree of orientation of the membranes in the stack, the correlation peak intensities were integrated as function of the meridonal angle φ (the angle relative to the q_z axis, see Fig-1.9). The corresponding intensity was fitted with a Gaussian distribution centered at zero, which was then used to calculate the degree of orientation using Hermans orientation function:

$$H = \frac{3\langle\cos^2\delta\rangle - 1}{2}. \tag{1.27}$$

where δ is given by the width of the Gaussian distribution.

Experimental Error

The experimental errors were determined as follows: Errors for peak positions, peak width and peak height are determined as the fit standard errors, corresponding to 95% confidence bounds, equivalent to twice the standard deviations, σ. Errors for calculated parameters, such as peak area, were then calculated by applying the proper error propagation [1].

1.2. Total Internal Reflection Fluorescence Microscopy (TIRF)

Microscopy is one of the main imaging techniques in biology. It allows to analyze the structure, composition and dynamic of cellular systems.
Since the development of optical microscopes at the beginning of the 17th century, these devices were used to investigate the principles of life. The first investigations focused on small animals such as insects and the microscopes exhibited a limited resolution. Before the first theoretical description of microscopical imaging by Ernst Abbe (19th century), the conditions for high resolution microscopy was most widely not understood.
Abbe discovered, that the resolution of classical optical microscopes is limited by the Rayleigh criteria, which describes the ability of an optical setup to distinguish two light-sources with a distance d. For microscopes this condition is given by [32]:

$$d_{max} = \frac{\lambda}{2n\sin(\alpha)} = \frac{\lambda}{2NA}, \tag{1.28}$$

where λ is the wavelength, n is the refraction index and α is the opening angle of the incident cone of light collected by the objective. The highest numerical aperture (NA) is achieved with an oil immersion objective, where the gap between the sample-slide and the objective lens is filled with an immersion oil. This leads to a NA up to 1.51 [33], which results in a maximum resolution of ~200 nm perpendicular to the optical axis and ~700 nm parallel to the optical axis.

The setup of a modern epifluorescence microscope is depicted in Fig. 1.10. This microscope has two light sources: the diascopic illuminator for the bright-field illumination and the episcopic illuminator for the epifluorescence illumination (ex-

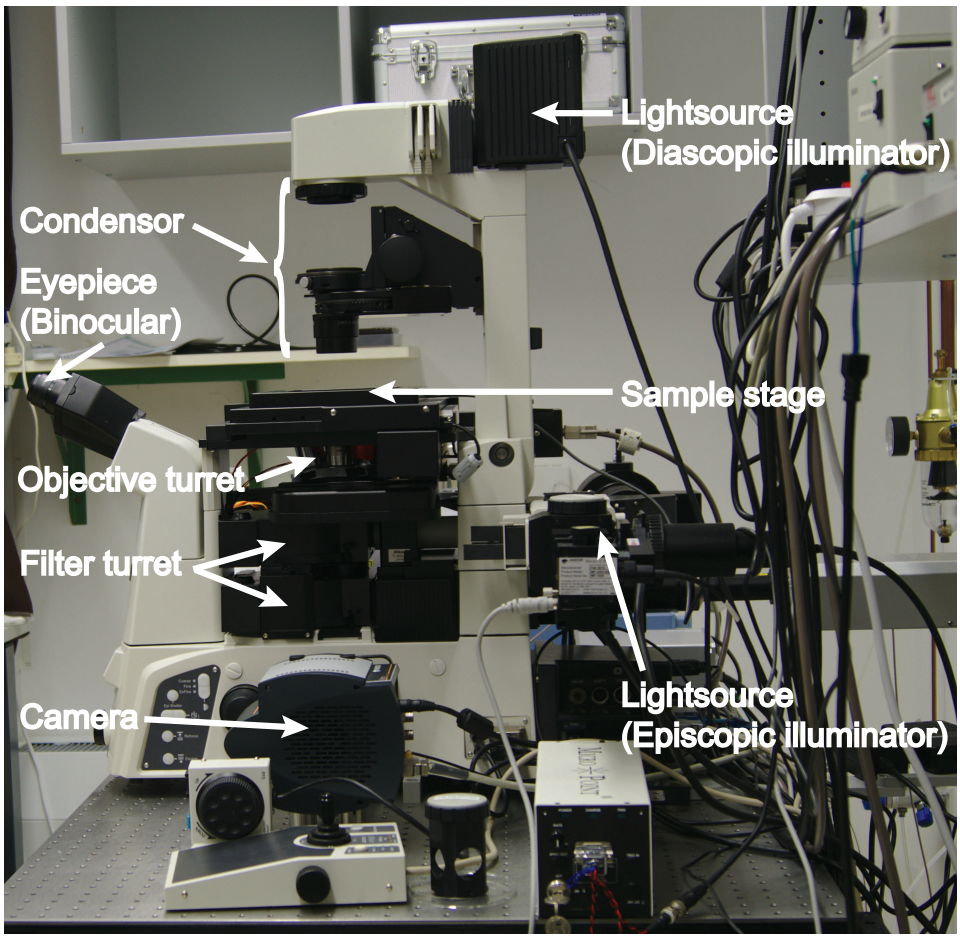

Figure 1.10.: Setup of a modern epifluorescence microscope.

citation). The diascopic illuminator illuminates the sample via the condensor, a set of lenses, which ensure a homogeneous illumination. The sample is mounted on a sample stage, which allows a mechanical manipulation of the position relative to the beam. The objective is a set of lenses which gather the light and produces a magnified real image of the specimen. This real image can be observed either via the eyepiece or a camera for further analysis. Multiple objectives are mounted on a objective turret providing an easy change of the objective during the measurement. For the epifluorescence mode, the epifluorescence illumination illuminates the sample with monochromatic light. The sample itself has to be stained with fluorescent dyes. Such dyes become excited by light with a certain wavelength λ and emit light with a slightly different wavelength (see Fig 1.11c)). A filter in the optical path between the dichroic mirror and the eyepiece/camera allows to filter out the excitation light. Hence, only the emitted light is transmitted.

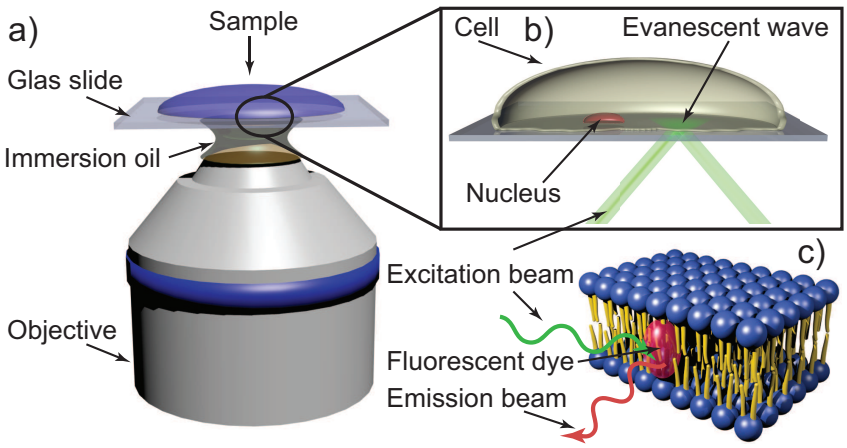

Figure 1.11.: Schematic setup of an TIRF microscope. a) A laser is focused by an oil immersion objective. b) The laser is incident on the object plate under an angle $\Theta > \Theta_c$ and becomes totally reflected. TIRF microscopy uses the evanescent wave to excite the dye in the labeled specimen

Epifluorescence microscopy is one method to increase the contrast of the microscope, compared to bright-field microscopy. Further, it allows to highlight certain cellular structures separately by labeling them with different dyes. There are multiple other techniques, such as phase contrast microscopy or dark-field microscopy, that provide an increased contrast.

There are various techniques, such as *Stimulated emission-depletion microscopy* (STED), *Stochastic optical reconstruction microscopy* (STORM) or *Total internal reflection fluorescence microscopy* (TIRF), that allow to increase the resolution limit given by Eq. 1.28. In this thesis, bright-field and epifluorescence microscopy is used to investigate the shape and the composition of RBC ghosts. While bright-field microscopy only allows to analyze the shape, epifluorescence microscopy offers a higher contrast and an analysis of the composition by labeling different molecules. Although the investigations were performed on a TIRF setup, the microscope was operating in the epifluorescence mode. However, the setup of a TIRF microscope will be explained briefly. The setup of an TIRF microscope is shown in Fig. 1.11 a). A laser beam is focused by an oil immersion objective and is totally reflected on the cover slide (Fig 1.11b)). If a light beam incident the interface between two optical media, it gets refracted according to Snell's law. Beyond an angle θ_c, also known as the critical angle, the light gets totally reflected on the interface. The solution of the Maxwell equations indicates that there is also a transmitted fraction

beside the dominant reflected fraction of the beam. This transmitted fraction is called the *evanescent wave*. This near field wave decays exponentially in the new material and is strong up to $\frac{1}{2}\lambda$ inside of the medium.
TIRF microscopy uses this evanescent wave to increase the resolution along the z-axis. The observed cells are first labeled with fluorescent dyes. Because of the exponential decay of the evanescent wave, this technique illuminates only specimen attached to the glass surface of the cover slip.
The images presented in this thesis were acquired through a LEICA DMI6000 B inverted microscope equipped with a Spectral Laser Merge Module for multi-wavelength illumination (Spectral, Richmond Hill, ON), adaptive focus control, a motorized X-Y stage (MCL Micro-Drive, Mad City Labs Inc., Madison, WI), a piezo X-Y-Z stage (MCL Nano-Drive, Mad City Labs Inc., Madison, WI), a LEICA 100x/1.47NAoil-immersed TIRF objective and an Andor iXon Ultra EMCCD camera. Excitation was provided by 488 and 647 nm diode-pumped solid-state lasers with 40 mW and 60 mW output power, respectively (Spectral, Richmond Hill, ON).

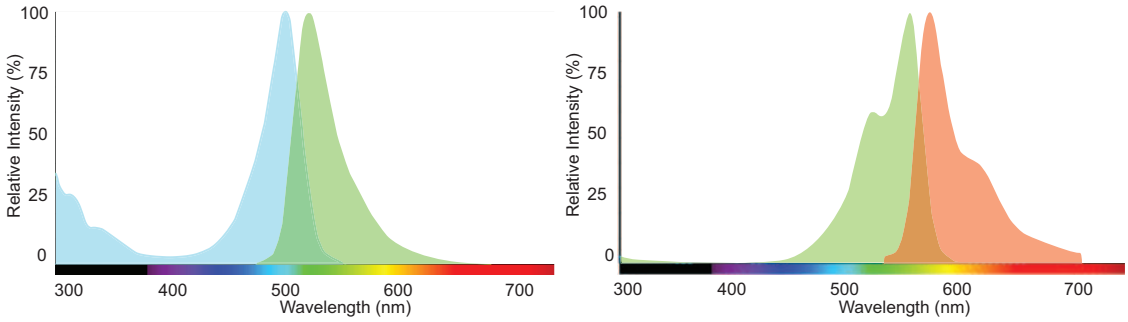

Figure 1.12.: a) Excitation spectrum (blue) and emission spectrum (green) for AlexaFluor 488-phalloidin. b) Excitation spectrum (green) and emission spectrum (red) for 1,1'-Dioctadecyl-3,3,3',3'-Tetramethylindocarbocyanine Perchlorate. (Spectra adapted from [34]).

AlexaFluor 488-phalloidin (Invitrogen, Life Technologies, Burlington, ON) was utilized to stain the actin filaments within the cells so that these structures may be visualized with the fluorescence microscope. To stain actin filaments, the RBC membranes were first permeabilized using a 0.2% Triton-X 100 solution in ultra-pure water with an incubation of 5 minutes. The substrates were then washed with ultra-pure water, and 5 μL of stock phalloidin in 200 μL of ultra-pure water was added to each sample and incubated for 20 minutes at room temperature. Then, the staining solution was replaced with ultra-pure water. In order to avoid a shrink-

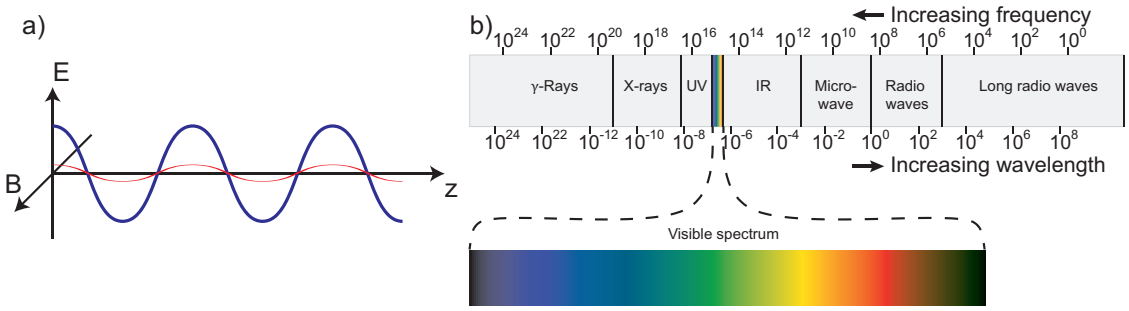

Figure 1.13.: a) Light propagate as electromagnetic wave, where the electric field vector $\vec{E}$ is perpendicular to the magnetic field vector $\vec{B}$. b) The spectrum of electromagnetic waves ranges from 10^7 m to less than 10^{-15} m. The visible spectrum ranges from 380 nm to 750 nm (Figure adapted from [36])

ing of the ghost vesicles because of the osmotic pressure, ultra-pure water was used instead of PBS, as proposed in the original protocol. The emission and excitation spectrum for AlexaFluor 488-phalloidin is shown in Fig. 1.12 b). Because the camera that was used records gray scale images, the images were colorized green afterwards, in order to mimic the emitted green light.
1,1'-Dioctadecyl-3,3,3',3'-Tetramethylindocarbocyanine Perchlorate (Sigma-Aldrich) was used to label the membranes. This lipophilic dye enters the membrane and propagates via lateral diffusion. The emission and excitation spectrum is presented in Fig. 1.12 a). To stain the RBC membranes, the protocol proposed in [35] was used [1].

1.3. UV-vis Spectroscopy

Ultraviolet–visible (UV-vis) spectroscopy is a common technique in biological research. It allows to analyze the composition of biological samples by measuring the absorption of light by the sample.

It is widely known that light propagates as electromagnetic wave, where the electric field vector $\vec{E}(\vec{r},t)$ is perpendicular to the magnetic field vector $\vec{B}(\vec{r},t)$ as sketched in Fig 1.13 a). The spectrum of electromagnetic waves ranges from wavelengths of

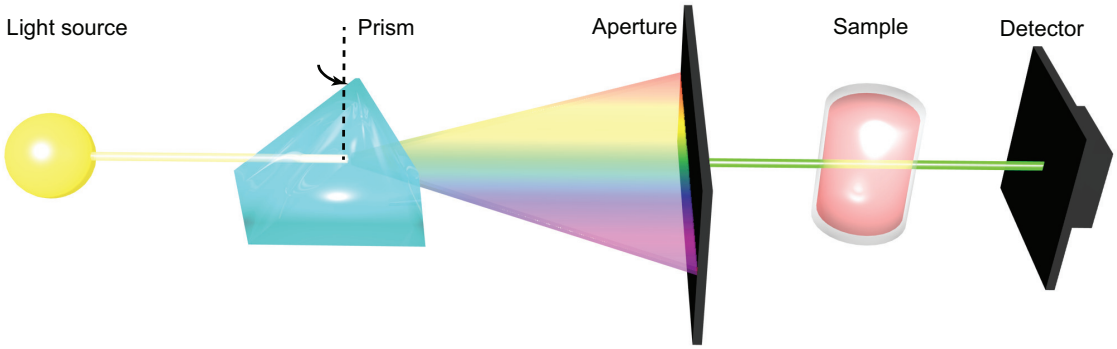

Figure 1.14.: Schematic illustration of an UV-vis Spectrometer. The sample is illuminated by monochromatic light and the transmitted light intensity is measured by the detector. The monochromator is illustrated with a prism and an aperture. (Figure from [1])

10^7 m, such as *Extremely Low Frequency* (ELF) waves, to less than 10^{-15} m, such as γ-rays [36]. The electromagnetic spectrum is depicted in Fig 1.13 b). Light can interact with matter in different ways: light can be scattered on particles, molecules can absorb the light, it can be reflected or transmitted. UV-vis spectroscopy uses the characteristic absorption spectrum of light in the visible and near UV- and infrared range to determine the composition of a sample and the concentration of certain molecules in the sample.

When absorbing electromagnetic energy, organic molecules become excited, *i.e.* the electrons can undergo a transition from a molecular orbital (MO) with a low energy to a MO with higher energy. UV and visible electromagnetic waves have just enough energy to induce transitions from nonbonding MO's to antibonding π^* MO's ($n \rightarrow \pi^*$) and from binding π MO's to nonbinding π^* MO's ($\pi \rightarrow \pi^*$) [37].

The absorption (extinction) of light by a certain organic molecule can be described by the *Lambert-Beer law* [37]:

$$E_\lambda = \epsilon_\lambda c d, \tag{1.29}$$

where E_λ is the extinction, *i.e.* the absorption of light with the wavelength λ, ϵ_λ is the substance-specific extinction coefficient, c is the concentration of the substance and d is the distance the light traveled in the substance. The molar extinction E_λ is characteristic for each organic substance and is defined as the extinction for a concentration of 1 $\frac{\text{mol}}{\text{l}}$ [37]. UV-vis spectroscopy was obtained using a M1000Pro Plate reader from Tecan. The technique is depicted in Fig. 1.14: The setup illuminates

the sample with monochromatic light using a Quad4 monochromator (illustrated with a prism and an aperture). The absorption of light in the visible and adjacent (near-UV and near-infrared) ranges is detected for wavelengths between 250 and 800 nm. Hemoglobin shows characteristic absorption lines at 335 ± 0.4 nm, 416.4 ± 0.2 nm 543 ± 0.8 nm and 577 ± 0.4 nm [38]. In order to prepare a sufficiently diluted RBC solution, 50 μL of the erythrocytes fraction was mixed with 1 mL phosphate-buffered saline (PBS). 400 μL of this solution was afterwards diluted with 400 μL PBS. This dilution procedure has been repeated three times. For the measurement, a 96-plate from Costar was used. 200 μL of the diluted blood solution, the ghost solution and the RBC solution were filled in the chambers of the plate. The absorption spectrum for each sample was scanned for wavelengths between 310 nm and 800 nm. In order to analyze the recorded spectrum, the data were fitted with a superposition of Gaussian peaks and the detected signals were integrated. The integrated peak intensity is related by 1.29 with the concentration of the analyzed substance [37]. Hence, the relative reduction of hemoglobin was determined by calculating the difference between the absorption spectrum of diluted RBC solution and the spectrum of the ghost solution respectively the sonicated ghost solution [1].

2. Red Blood Cells and their Membranes

Blood is one of the main fluids in the human body. It transports nutrients and oxygen, regulates the temperature and the pH, and is part of the immune defense. The main component of blood are the red blood cells (RBCs), which are commonly used in biophysical research because of their relatively simple structure [39, 40, 41, 42, 43, 44]. In this thesis, the molecular structure of RBC membranes was investigated, using X-ray diffraction. The membranes were extracted from the RBCs and dried on silicon wafers in order to prepare highly ordered, solid supported stacked RBC membranes. Further, the effect of the common drug aspirin on this structure was investigated. The following chapter gives an introduction in the known structure of RBCs with focus on their membranes and the known interactions between RBCs and aspirin.

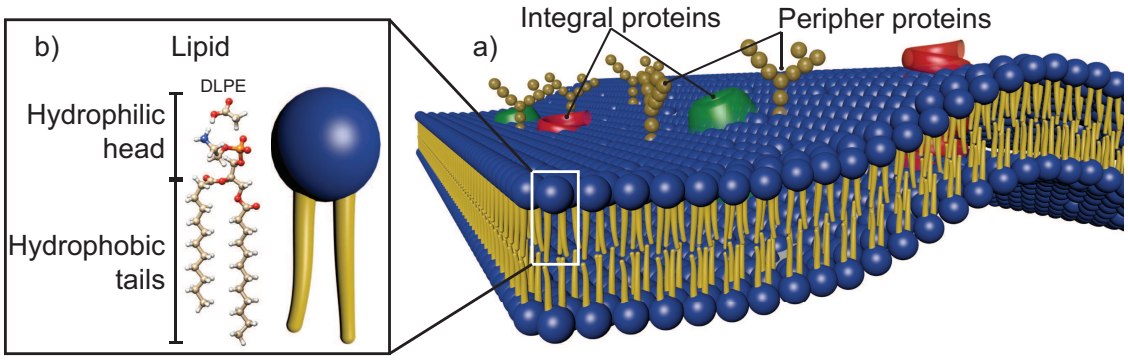

Figure 2.1.: a) Schematic illustration of a lipid bilayer. The amphiphilic lipid molecules consist of a hydrophilic head group and hydrophobic tails. (b) Various kinds of proteins, such as channels, transporters, receptors, linkers and enzymes are embedded in the bilayer.

2.1. Biomembranes and Osmosis

The structure of biomembranes is illustrated in Fig. 2.1. They typically consist of a phospholipid bilayer with embedded proteins (Fig. 2.1 a))[41, 45]. The structure of a lipid molecule is sketched in Fig. 2.1 b). Those molecules consist of a hydrophobic head and hydrophilic tails. This amphiphilic structure causes the formation of lipid bilayers: In order to minimize the energy, the hydrophilic tails of the two monolayers face each other such that only the head groups are in direct contact with the surrounding water. Beside lipid molecules, biomembranes can include cholesterol. While bacterial membranes have no cholesterol, the fraction of cholesterol in animal cells can be up to 50%[41]. One can differ two types of proteins: integral proteins and peripher proteins [41]. Integral proteins have an amphiphilic structure and are permanently embedded in the membrane. This protein class includes various different protein types, such as linkers, enzymes, transporters, channels and receptors. In contrast, peripher proteins are attached either to lipids or to integral proteins and include linkers, enzymes and structural proteins, such as the cytoskeleton [41].

Since decades, lipid bilayers are in the focus of biophysical research with respect to the structure and the dynamic of lipid molecules and lipid domains [8, 46, 47, 48]. The physical state of a lipid bilayer is defined by the fluidity of the membrane. Two different states are differentiated in the literature [1, 41]: the *liquid disordered* (or fluid) state and the *gel* state. In the liquid disordered state the bilayer is characterized as a liquid crystal like structure. Each lipid has more space in the bilayer, resulting in a higher degree of rotational freedom as well as for lateral transitions. This liquid disordered state undergoes a transition to the gel state below a critical temperature T_c. This temperature depends on the lipid molecule present in the bilyer. The more unsaturated bonds the lipid tails have, the lower is this critical temperature [41].

A native cell membrane consists out of several different lipid molecules. These molecules are not equally spread through the bilayer but form domains, *i.e.* functional regions made of sphingolipids and cholesterol. Since these lipid rafts were first postulated by Stier and Sackmann [49] and Klausner and Karnovsky [50], these domains were mainly investigated by analyzing the structure of artificial bilayers [25, 30, 41, 51, 52, 53, 54, 55]. Although artificial membranes show domains of sphingolipids and cholesterol, it is an ongoing discussion among scientists whether lipid rafts exist in native cells or not. While recent studies by Ciana *et al.* [56] and

Mikhalyov *et al.* [57] present evidence for lipid rafts in human RBCs, the size of such functional domains is expected to be small (10 - 25 nm)[41].
The structure of a lipid bilayer results in a semipermeable membrane, which allows a highly selective material exchange. While smaller molecules, such as water, can diffuse through the membrane, ions and larger molecules such as glucose need active transport through the bilayer. The diffusion of water through such a semipermeable membrane is called *osmosis* [58]. The direction of the osmosis strongly depends on the concentration of osmotic active particle, such as ions, on both sides of a membrane. One can define the osmolarity of a solution by $b_{osm} = \frac{n_{osm}}{V_{sol}}$, which describes the concentration of osmotic active molecules in a solution. The water transport is always from a low to a high osmolarity. The system is in the steady state when the osmolarity is equal on both sides of the membrane. One can easily understand this effect as an entropically driven transport. One considers two phases separated by a semipermeable membrane: one phase consists out of pure solvent (phase 1),*e.g.* water, and the second phase consists out of a salt solution (phase 2),*e.g.* NaCl in water. The volume of both phases is identical. The membrane limits the phase space for the salt ions in the solution. However the entropy of the whole system can be maximized by an influx of solvent from phase 1, *i.e.* the phase with the lower osmolarity, to phase 2, *i.e.* the phase with the higher osmolarity.
Osmosis is the most important passive transport in biology. Hence, the difference in osmolarity between the intercellular and intracellular medium is important for the cellular functionality. One can differ three environments [58]: a hypertonic, an isotonic and a hypotonic solution. In case of a hypertonic solution, the salt concentration of the intercellular medium is higher than the one of the intracellular medium. Hence, water flows out of the cell and the cell shrinks. On the other hand, a hypotonic solution results in an influx of water, caused by a lower salt concentration of the intercellular medium. In case of an isotonic solution, the salt concentration both inside and outside of the cell is equal.

2.2. The Structure of Red Blood Cells

Blood is one of the most important fluids in the body of mammals and non-mammalian vertebrates. This thesis focuses on human blood which is comparable to that of other mammals.
It consists of two main components: the plasma and cellular components. The

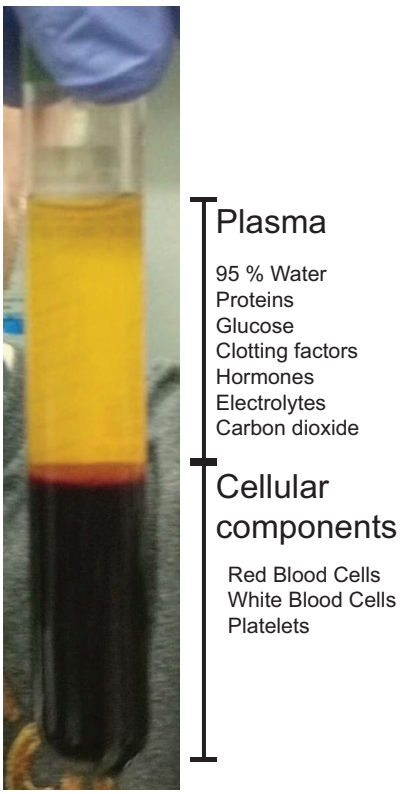

Figure 2.2.: Blood sample after centrifugation at 3,000 g. A clear separation between a plasma fraction and a cellular fraction is observed. The plasma fraction consists mostly of water and the cellular fraction mostly of red blood cells. White blood cells and platelets form a thin layer between both fractions.

plasma contains mostly water (~95%) as well as proteins, glucose, clotting factors, electrolytes, hormones and carbon dioxide [59]. There are three cell types that can be found in human blood: white blood cells, red blood cells (RBCs) and platelets. The white blood cells play an important role in the mammal immune system. Platelets mainly control the blood coagulation. Hereafter we focus on the third cell type: the RBCs, which represent the majority of the cellular components (99% [59]). The fraction of RBCs on the blood is also called hematocrit. Human RBCs are significantly smaller than other human cells. Healthy RBCs have a characteristic discocyte shape as depicted in Fig. 2.3 a) and b). The cells have a diameter between 6.2 and 8.2 μm and a thickness between 2 and 2.5 μm at the thickest point and between 0.8 and 1 μm at the thinnest point [60]. The volume of an RBCs varies between 90 fL and 150 fL [61].

The shape of RBCs can vary for different environments. As described above, the osmolarity of the intercellular medium strongly effects the water diffusion through the cell membrane. RBCs in a hypotonic solution swell because of the inflowing water. Those RBCs are called stomatocytes. If the osmotic pressure is too high, the cell membrane bursts. The resulting empty vesicles are called RBC ghosts, based on their appearance under the microscope. On the other hand, RBCs in a

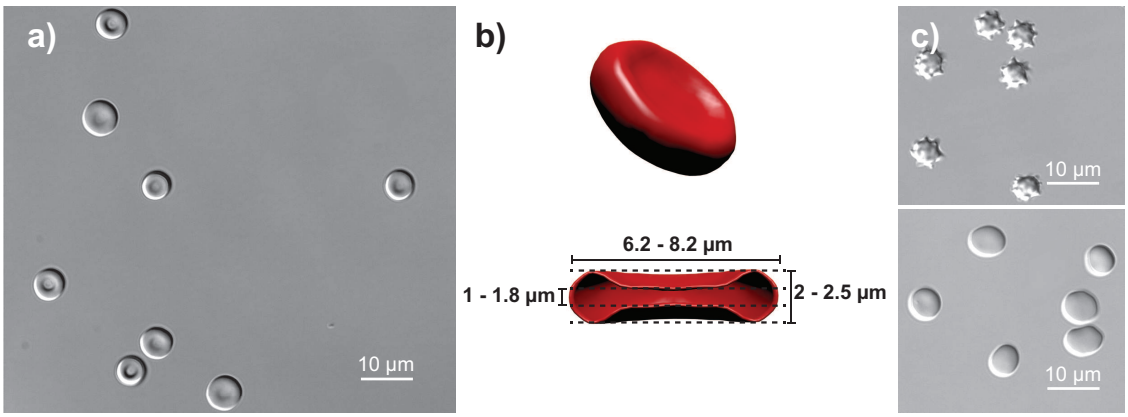

Figure 2.3.: a) Microscopic immages of RBCs. The cells show a discocyte shape. b) Schematic illustration of shape and structure of an RBC. The cells have a discocyte shape, an diameter between ~ 6.2 to 8.2 μm and a thickness between 2 and 2.5 μm on the thickest point and 1 to 0.8 μm at the thinnest point c) RBCs can show different shapes depending at the osmolarity of the surrounding medium. A hypotonic solution results in spherozytes (lower picture), a hypertonic solution results in echinozytes (upper picture).

hypertonic solution shrinks and form echinocytes (see 2.3 c)).

Compared to other cells, RBCs have a relatively simple structure. They have no nucleus and complex organelles like mitochondria [62]. This simplicity makes them useful for biophysical research, although it results in physiological peculiarities. The absence of mitochondria for instance, prohibits the synthesis of ATP by the cell. Hence, energy has to be provided by glucose [63]. The inner volume of RBCs is dominated by hemoglobin, which causes the red appearance of the cells [62]. Because of this iron-containing metalloprotein RBCs are able to transport oxygen from respiratory organs to the rest of the body. This thesis focuses on the membrane of RBCs which consist of three layers [67, 68]. The glycocalyx layer, the lipid bilayer, and a protein network, *i.e.* the cytoskeleton, attached to the inner side of the lipid bilayer. From all membranes in nature, the RBC membrane is the most studied one [67]. It is reported to consist of phospholipids and cholesterol in equal proportions of weight [68]. Among others, there are five main lipid types found in RBC bilayers. The outer monolayer contains mainly Phosphatidylcholine and Sphingomyelin. The inner monolayer contains mainly Phosphatidylethanolamine, Phosphoinositol, and Phosphatidylserine. Cholesterol is found in both monolayers [68]. It was previously reported, that RBC membranes consist of ~52 % proteins and ~40 % of lipids (including cholesterol)[69]. An overview over the main proteins

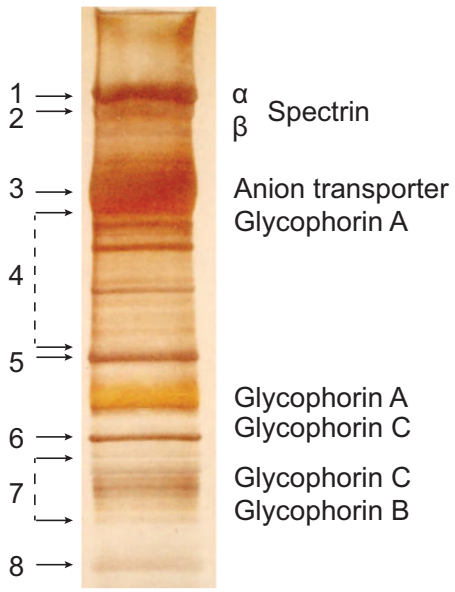

Figure 2.4.: a) SDS page of a RBC membrane. This method seperate the proteins by their molecular mass. A description of the protocol can be found in [64, 65] (Figure from [66]).

in RBCs can be found in [68, 70]. Fig. 2.4 a) presents a SDS-page of the RBC membrane proteins. This procedure allows to seperate proteins by their molecular mass. A description of the protocol can be found in [64, 65]. The presented SDS-page indicates that the cytoskeleton of RBC consists mainly of spectrin and actin fibers. Those proteins are connected via the Band 3 membrane protein, which is the main integral protein, found in RBC membranes [67, 71].

2.3. Interaction between Aspirin and Red Blood Cells

The solid supported RBC membranes presented in this thesis offer on the one hand a detailed study of the structure of those membranes and on the other hand the analysis of structural effects of drugs on membranes. Modern drugs typically interact with specific protein structures. However, there is a growing evidence for an interaction of various pharmaceuticals with lipid bilayers, leading to structural and stability changes [72]. In particular, non-steroidal anti-inflammatory drugs (NSAID's) have been shown to disturb bilayer structures in native and model membranes [7, 73]. Aspirin is certainly one of the most common NSAID's [1, 4, 73]. Aspirin is the trade name for acetylsalicylic acid (ASA), whose molecular structure is sketched in Fig. 2.5.

When present in the body, ASA binds and inactivates cyclooxygenase and suppresses the production of prostaglandin and thromboxanes. While high doses ASA

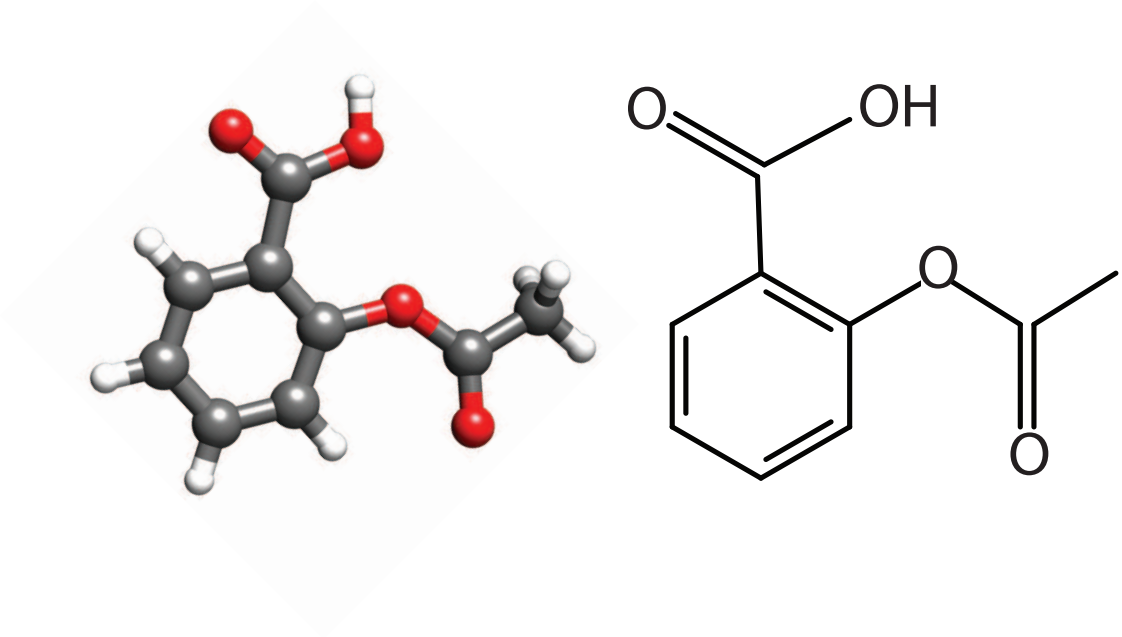

Figure 2.5.: Structure of acetylsalicylic acid (ASA)

shows anti-inflammatory effects, low doses ASA are believed to inhibit COX-1 and act on COX-2, resulting in a lower platelet activity, which are involved in the formation of blood clots [74, 75]. However, aspirin is also known to interact with lipid bilayers. It strongly perturbs model membrane structure in a concentration dependent manner and also influences human erythrocyte shape [76]. It decreases the hydrophobic surface barrier in mucosal membranes, leading to a diffusion of acid and gastrointestinal injury [6] and impacts on protein sorting [77]. Aspirin was previously reported to partition in lipid bilayers and positions itself in the lipid head group region [3, 4, 19]. Recently, an interaction between aspirin and cholesterol was reported, as aspirin was observed to reduce the volume of cholesterol plaques in model membranes at elevated cholesterol concentrations of ~40 mol% [19]. Aspirin also inhibits the formation of cholesterol rafts in fluid lipid membranes at physiological cholesterol concentrations [1, 3, 19].

3. Preparation of Solid Supported Red Blood Cell Membranes

The preparation protocol is schematically depicted in Fig. 3.1 and consists of two main parts: In the first step, red blood cell (RBC) ghosts are produced from blood samples. In the second step, these RBC ghosts are applied onto silicon wafers and annealed to form multi-lamellar RBC membrane stacks.

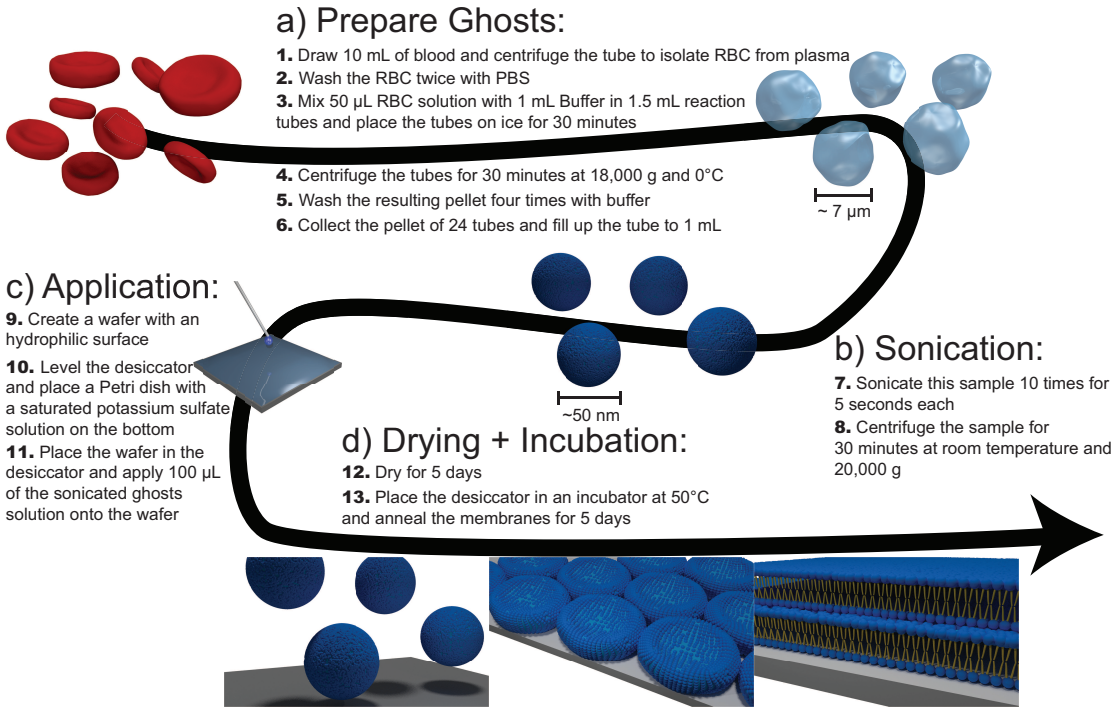

Figure 3.1.: Schematic of the Blood-on-a-chip preparation protocol. a) The protocol bases on the original prepatation protocol for RBC ghosts. b) The RBC ghosts are then sonicated to form nanometer sized vesicles. c) The sonicated solution is applied to a silicon wafer. d) The wafer is dried and annealed for several days to form well developed multi-lamellar stacks on RBC membranes on the silicon wafer (Figure from [1]).

3.1. Preparation of Red Blood Cell Ghosts

This thesis describes the structural analysis of RBC membranes from highly oriented multi-lamellar membrane stacks. Although the analysis method is common for artificial methods [4, 18, 78], it is difficult to adapt the technique for native cell membranes. Because of the complex structure of cells, it is difficult to properly separate the membrane from other cell compartments.
The preparation of RBC ghosts was first published in 1963 by Dodge, Mitchell and Hanahan [5]: 10 mL of venous blood were drawn from a participating individual. The blood was collected in venous blood collection tubes from BD (Product Number: BD 367874), coated with sodium heparin as anticoagulant. The tube was centrifuged at 3,000 g for 10 min at room temperature. After this process, a clear separation between an erythrocyte fraction and a plasma fraction was observed as shown in Fig. 2.2. The white blood cells and platelets form a layer between those two fractions. In the original protocol, the separated blood is then washed and filtered by a protocol presented in [5]. First, 1.8 g α-Cellulose and 1.8 g σ-Cellulose was diluted in 100 ml ultra pure water. Then, ~10 ml of this solution was filled in a syringe furnished with a filter paper on the bottom. While the water can pass the filter paper, the cellulose sediments on the bottom of the syringe. The setup is shown in figure 3.2 a). Two solutions were prepared from the centrifuged blood sample:

- Solution 1:
  1 ml plasma on 9 ml PBS

- Solution 2:
  1 ml hematocrit on 1 ml PBS

Those solutions were then successively filled in the syringe and passed through the filter: First 10 ml of solution 1 was filled in the filter, then 1 ml of solution 2. The filtrate was disposed. Finally the filter was washed with PBS and the filtrate was collected. While the leukozytes and platelets remain in the filter, the RBCs can pass the filter.
While this protocol is well established and widely used in blood cell investigations (see, for instance, [80] for a recent review), the ghost solution produced by this protocol did not result in well developed multi-lamellar membrane stacks when applied on silicon wafers. Cellulose particles were observed under the microscope

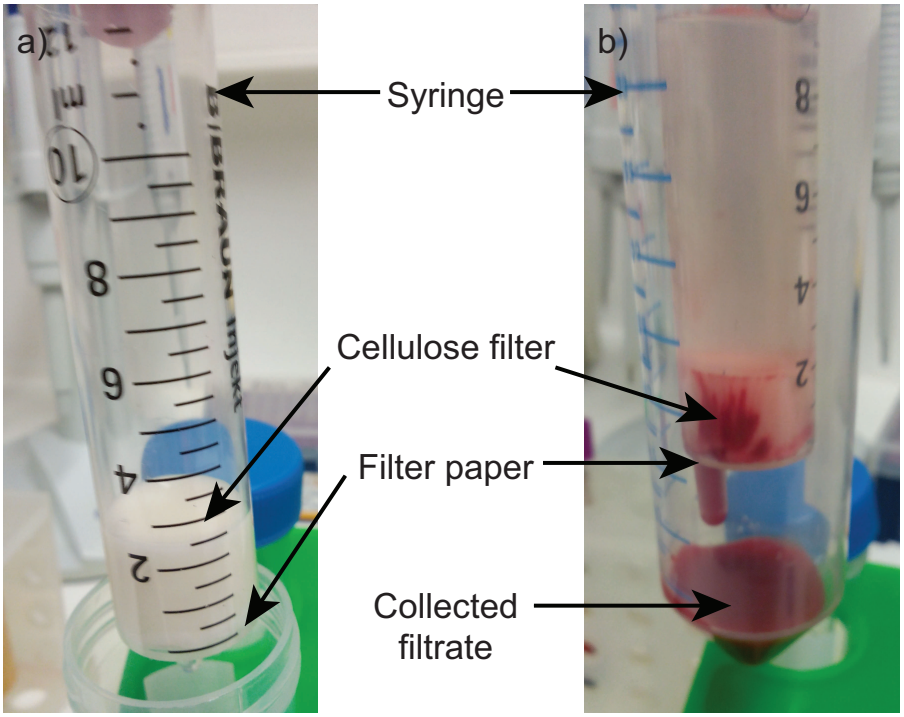

Figure 3.2.: Initially the blood was filtered referred to a protocol from Beutler, West and Blume [79]. a) 10 ml of a solution of 1.8 mg α- and σ-Cellulose in 100 ml ultra pure water was filled in a syringe furnished with a filter paper on the bottom. While the cellulose remains in the syringe, the water can pass the filter paper. b) 10 ml of solution 1 and 1 ml of solution 2 is pushed through the filter. Finally the filter is washed with 10 ml PBS and the filtrate is collected.

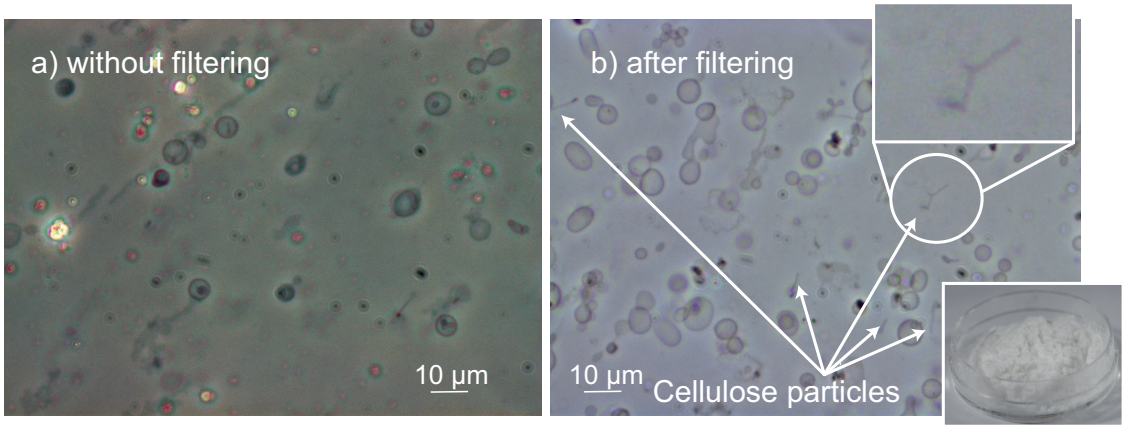

Figure 3.3.: The RBC ghosts were analyzed with birght-field microscopy. Cellulose particles were found in the solution prepared by the original protocol. (Figure from [1]).

in the solution after passing through the filter as depicted in Fig. 3.3. These likely inhibit the formation of well-ordered membrane stacks [1]. In order to avoid contamination with cellulose, the hematocrit was purified through centrifugation using the following protocol: The supernatant in the separated blood sample was removed using a pipette. PBS was added to the precipitate to achieve a volume of 10 mL and centrifuged at 3,000 g for 10 min. This process was repeated twice.
50 μL of the RBC solution was then mixed with 1 mL of buffer solution in a 1.5 mL reaction tube as shown in Fig. 3.4. For the buffer, 16 mL of PBS and 484 mL of 18.2 MΩ·cm ultra pure water were mixed and stored at 0°C. The solution was buffered with potassium hydroxide and hydrochloric acid to a pH of 8. This creates a hypotonic solution for the RBCs, resulting in an influx of water into the cells and their lysis as described in Chap. 2.1. The diluted solution is vortexed for 10 s to prevent clumping. After vortexing, the reaction tube is immediately placed in ice for 30 min to slow down the re-closing of the burst cells.
Samples were then centrifuged at 18,000 g for 30 min at ~0°C. After the centrifugation, a pellet is formed at the bottom of the reaction tube. The supernatant was removed by pouring the reaction tube in a beaker. 1 mL buffer solution was added to the pellet and the solution was vortexed for 10 s and centrifuged for 15 min at 18,000 g and ~0°C. This process of centrifugation and removal of the supernatant was repeated 4 times. During this washing, most of the hemoglobin is removed, resulting in a transparent, colorless solution. Fig. 3.5 a) shows images of the reaction

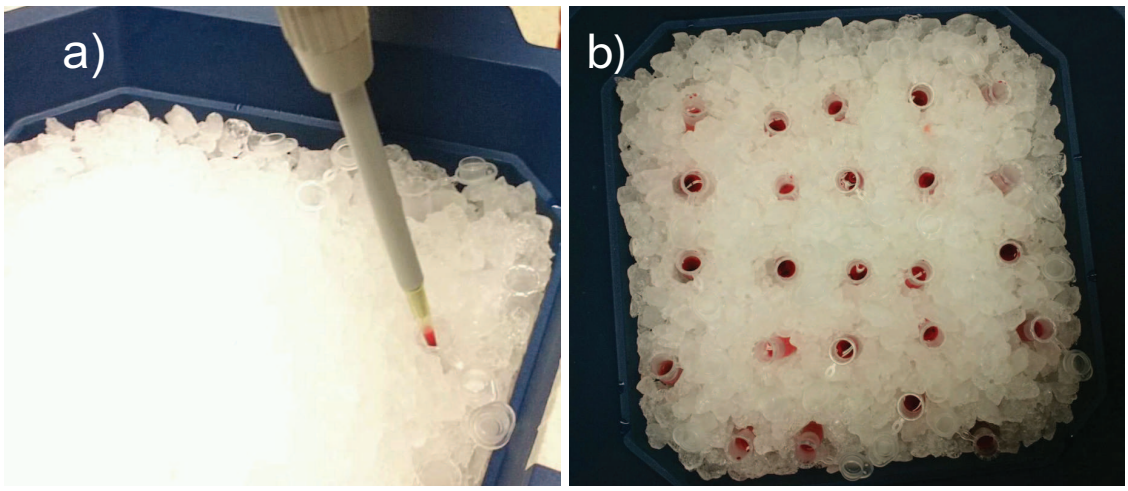

Figure 3.4.: a) 50 μL of the RBC solution was mixed with 1 mL of buffer solution in a 1.5 mL reaction tube. b) The samples were vortexed for 10 s to avoid clumping and the tubes were immediately placed on ice for 30 min.

tube after different numbers of washing steps.

The removal of hemoglobin was quantitatively checked using ultraviolet–visible spectroscopy (UV-vis). The corresponding data is shown in Fig. 3.5 b). The characteristic hemoglobin absorption bands at 335 nm, 416.4 nm, 543 nm and 577 nm [38] decrease in every step; the hemoglobin content of the final solution was found to contain less than 2% of the original content.

This procedure results in solutions with a typical mass concentrations of RBCs of ~0.3 mg/mL. To increase the concentration, pellets from 24 such reaction tubes were collected and centrifuged at 18,000 g for 15 min. The supernatant was removed and the tube was refilled with buffer solution to the 1 mL mark of the tube. This results in a solution with a final mass concentration of ~7 mg/mL. The ghost solution was analyzed by fluorescence microscopy, as shown in Fig. 3.6 a) and b). The RBC membrane was fluorescently labeled in part a) using 1,1'-Dioctadecyl-3,3,3',3'-Tetramethylindocarbocyanine Perchlorate (DiI). The image shows a mix of multi-lamellar and uni-lamellar ghosts with a highly irregular shape and a large distribution of shapes and sizes, from round to long, more chain-like objects including vesicles that contain several smaller vesicles. These shapes are likely related to the presence of a cytoskeleton, whose main components are spectrin and actin in RBCs as described in Chap. 2.2. To analyze this network, Alexa Fluor 488 labelled phalloidin was used to label the F-actin network in Fig. 3.6 b). Structures of ~5 μm were observed, indicative of the presence of actin.

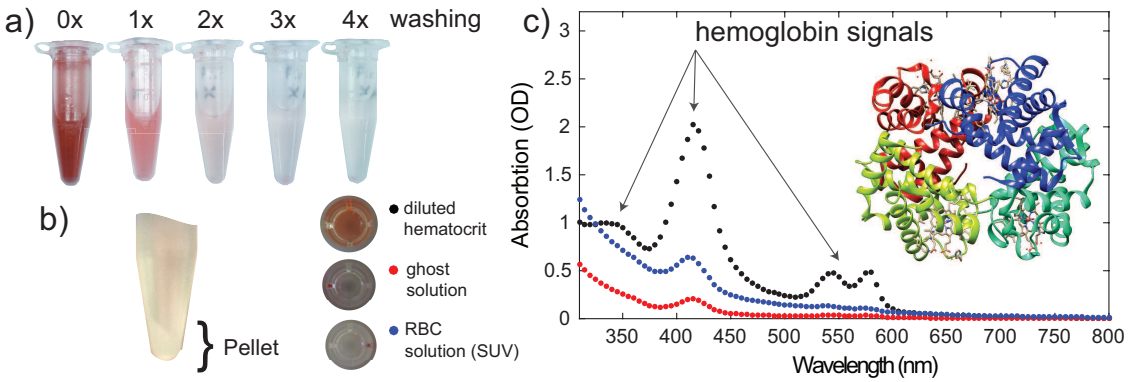

Figure 3.5.: a) The reaction tube after different numbers of washing steps. The disappearance of the red color indicates the hemoglobin removal. b) Final result of the ghost protocol. The empty RBC vesicles are sedimented in a pellet on the bottom of the tube. c) The hemoglobin concentration was quantitatively checked by UV-vis spectroscopy. (Figure from [1])

As indicated below, the variation in size and shape of the ghosts, and the presence of actin filaments likely prevents the formation of well defined, solid supported multi-lamellar RBC membranes. To achieve a more uniform distribution of vesicle sizes and shapes, the RBC solution was tip sonicated 10 times for 5 s, each, in order to form small uni-lamellar vesicles (SUVs). The result of the sonication process is shown in Fig. 3.6 c) and d). In part c), the membrane was fluorescently labeled using DiI. Small dots were observed, indicative of small uni-lamellar vesicles of ~50 nm, beyond the resolution limit of the microscope.

The actin concentration was analyzed by staining with Alexa Fluor 488 labelled phalloidin. After sonication, no more particles were observed within the resolution of the microscope used. In order to separate the SUVs and remaining actin, the solution was centrifuged for 30 min at 20,000 g. Since SUVs can only sediment in ultracentrifuges at 120,000 g when centrifuged for more than 30 min [81], the pellet contains actin polymers and potentially larger and multi-lamellar vesicles, while the SUVs stay in the supernatant. This supernatant was found to be ideal for the formation of solid supported, multi-lamellar RBC membranes, as will be discussed below.

3.2. Silicon Wafer Preparation

All membranes were prepared on single-side polished silicon wafers. 100 mm diameter, 300 μm thick silicon wafers were pre-cut into 10×10 mm^2 chips. The wafers were functionalized for deposition of the ghost solution by either preparing a hydrophobic or hydrophilic surface.
To create a hydrophobic silicon surface, the wafers were pre-treated by sonication in dichloromethane (DCM) at 40°C for 25 min. This treatment removes all organic contamination and leaves the surface in a hydrophobic state. Each wafer was then thoroughly rinsed three times by alternating with ~50 mL of ultra pure water with a resistivity of 18.2 MΩ·cm and HPLC grade methanol.
To create a hydrophilic state, the wafers were cleaned by immersion in an $H_2O_2^+$ sulfuric acid mixture (volume fraction of 70% concentrated H_2SO_4, 30% H_2O_2 at 40°C, Piranha solution) for 30 min on a 3D orbital shaker (VWR) set to tilt angle 1 and speed 15). This strongly oxidizing combination removes all organic contaminants on the surface, but does not disturb the native silicon oxide layer. Each wafer was then thoroughly rinsed with ~50 mL of ultra pure water with a resistivity of 18.2 MΩ·cm [1].

3.3. Fabrication of Highly Oriented, Multi-Lamellar Solid Supported Red Blood Cell Membranes

The ghost solution did not spread well on hydrophobic silicon wafers, as shown in Fig. 3.7 a). For this wafer, 100 μL of concentrated ghosts solution was applied onto a 10×10 mm^2 hydrophobic silicon wafer mounted on a leveled hot plate at a temperature of 40°C. The solution was applied slowly using a 100 μL syringe to avoid spill, and the wafer typically dried within ~10 min. The membrane film was found not to cover the entire wafer and showed several wrinkles.
Slowly drying the solution to allow more time for the solution to spread and membranes to form was achieved by placing the wafers in a leveled desiccator for 5 days at 97.6±0.5 % relative humidity using a saturated K_2SO_4 salt solution. The slow drying resulted in a smoother film, however, still incomplete coverage of the substrate, as shown in Fig. 3.7 b).
Fig. 3.7 c) shows a hydrophilic wafer prepared by applying 100 μL of concentrated SUV solution and dried for 5 days at 97.6±0.5 % relative humidity. The solution

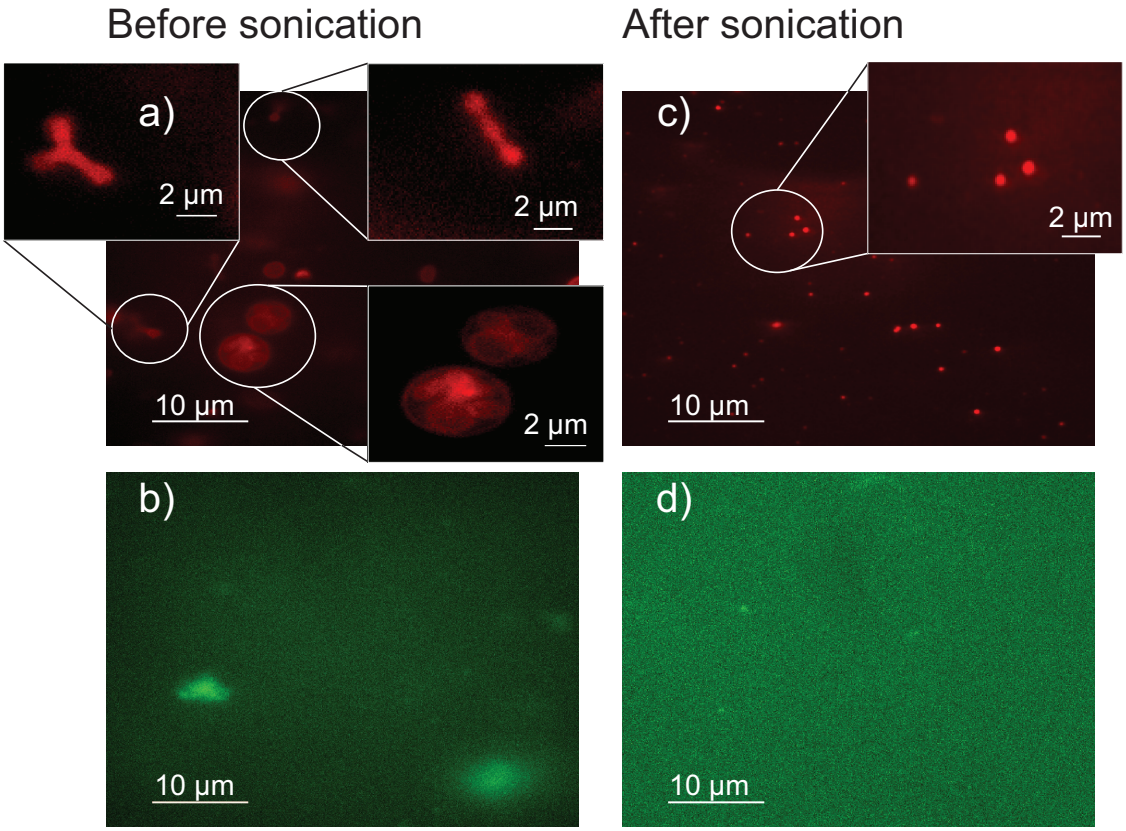

Figure 3.6.: Fluorescence microscopy images of the ghost solution before and after sonication. The membrane was labelled using DiI in parts a) and c), while Alexa Fluor 488 labelled phalloidin was used to label the F-actin network in b) and d). Before sonication, ghosts of highly irregular shape and a large size distribution are observed including 'ghosts inside of ghosts'. The solution also contains large clusters of actin. Small vesicles with a uniform size distribution are observed after sonication and no actin particles (within the resolution of the microscope used). (Figure from [1]).

covered the entire wafer indicating a homogeneous mass distribution. However, only weak signals of membrane stacking were observed in this sample and one can picture the morphology of the membranes as depicted in Fig. 3.1 d), as uni-lamellar vesicles that have been dried out on the silicon substrate. This situation is similar to the preparation of single solid supported bilayers through vesicle fusion [82, 83], where small bilayer patches initially develop on the substrate, and eventually undergo a transition into a large uniform single bilayer [82]. Substrates are typically annealed for 72 h at 55°C in an oven in air. The energy barrier for forming a lamellar structure can be overcome through gentle heating and the lamellar membrane organization becomes energetically more favorable, as it minimizes the bending

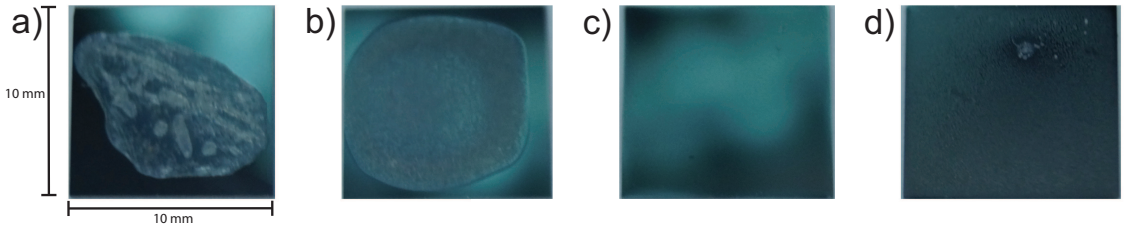

Figure 3.7.: a) Photos of the silicon chips after a) application of the RBC solution on a hydrophilic wafer and fast drying, b) application on a hydrophobic wafer after slow drying. c) and d) show hydrophilic wafers after slow drying and slow drying and annealing, respectively. See text for details. (Figure from [1]).

energy.

However, using the same procedure and heating the RBC membranes in an oven led to destruction of the membrane film. The silicon chips were, therefore, incubated at different temperatures and under relative humidities between 50% and 100% RH by placing them in a closed container and exposure to different saturated salt solutions. The best results were obtained when the RBC chip was annealed at 50°C and 95.8±0.5% relative humidity in a saturated K_2SO_4 salt solution for 5 days, which resulted in the photo in Fig. 3.7 d) [1]. In this protocol, annealing of the RBC membranes at high temperature and humidity leads to the formation of lamellar membrane structures through membrane fusion.

3.4. Preparation of Red Blood Cell/Aspirin Complexes

In order to prepare complexes of RBC membranes containing increasing amounts of aspirin, a solution of 9 mg/mL acetylsalicylic acid (molecular weight 180 g/mol) in 18.2 MΩ·cm water was prepared. 2 μL, 3 μL, 4 μL, 5 μL, and 6 μL of this solution were added to 100 μL of the final ghosts solution resulting in acetylsalicylic acid concentrations of 1 mM, 1.5 mM, 2 mM, 2.5 mM and 3 mM. The resulting solutions were applied onto silicon wafers and dried slowly and incubated for 5 days following the above protocol.

The molar concentration of ASA in the RBC membranes can be estimated as follows: between 2 and 5 μL of the 9 mg/mL ASA solution were added to the membrane solution, resulting in between $1{\cdot}10^{-7}$ and $2.5{\cdot}10^{-7}$ mol. 100 μL of the

7 mg/mL RBC solution contain ~$2 \cdot 10^{-6}$ mol (when assuming an average molecular weight of the membranes of 400 g/mol). This results in molar ASA concentrations between 5-10 mol%, *i.e.*, 1 ASA molecule per 10 to 20 lipid molecules [1]. This ASA concentration is elevated as compared to plasma concentrations of typically less than 1 mol%, however, comparable to ASA concentrations typically used in the literature [84].

4. Structure Analysis

4.1. Molecular Structure and Properties of Red Blood Cell Membranes

X-ray diffraction was used to determine the molecular structure of the RBC membranes. As the membranes were oriented with their membrane plane parallel to the silicon substrate, the in-plane and out-of-plane structure was determined separately, but simultaneously as described in Chap. 1.1.2. The organization of the membranes normal to the silicon wafer is observed along the q_z-axis, while molecular organization in the plane of the membranes, parallel to the substrate is observed along the $q_{||}$-direction. Fig. 4.1 shows the resulting 2D diffraction data and cuts along the q_z-axis for samples produced by different preparation protocols: Figs. 4.1 a) and b) show the data for the fast dried non-sonicated ghosts on hydrophobic and hydrophilic wafers respectively. The scans for slow dried and slow dried and annealed RBC solution on hydrophilic wafers are depicted in Figs. 4.1 c) and d). A lamellar membrane structure, *i.e.*, a stack of membranes, where the bilayers are organized parallel to each other, results in a series of equally spaced and well defined Bragg reflections in diffraction experiments [17]. While for fast and slow dried nonssonicated ghosts only weak signals were observed, the slow drying and especially the slow drying and annealing results in well developed prominent Bragg peaks. The sketches in Fig. 4.1 illustrate the corresponding model: drying of pure ghosts results in flat but not necessarily fused micrometer sized vesicles on the silicon surface. The slow drying and annealing supports the fusion of the small nanometer sized vesicles observed for the sonicated solution. The result for the protocol described in Chap. 3 will be discussed in the following paragraphs.
Fig. 4.2 b) shows typical 2-dimensional X-ray diffraction data resulting from wafers produced by the protocol described in Chap. 3. Cuts of the diffracted intensity along the out-of-plane and in-plane direction are shown in Figs. 4.2 c) and d). By analyzing out-of-plane and in-plane patterns, the corresponding signals were

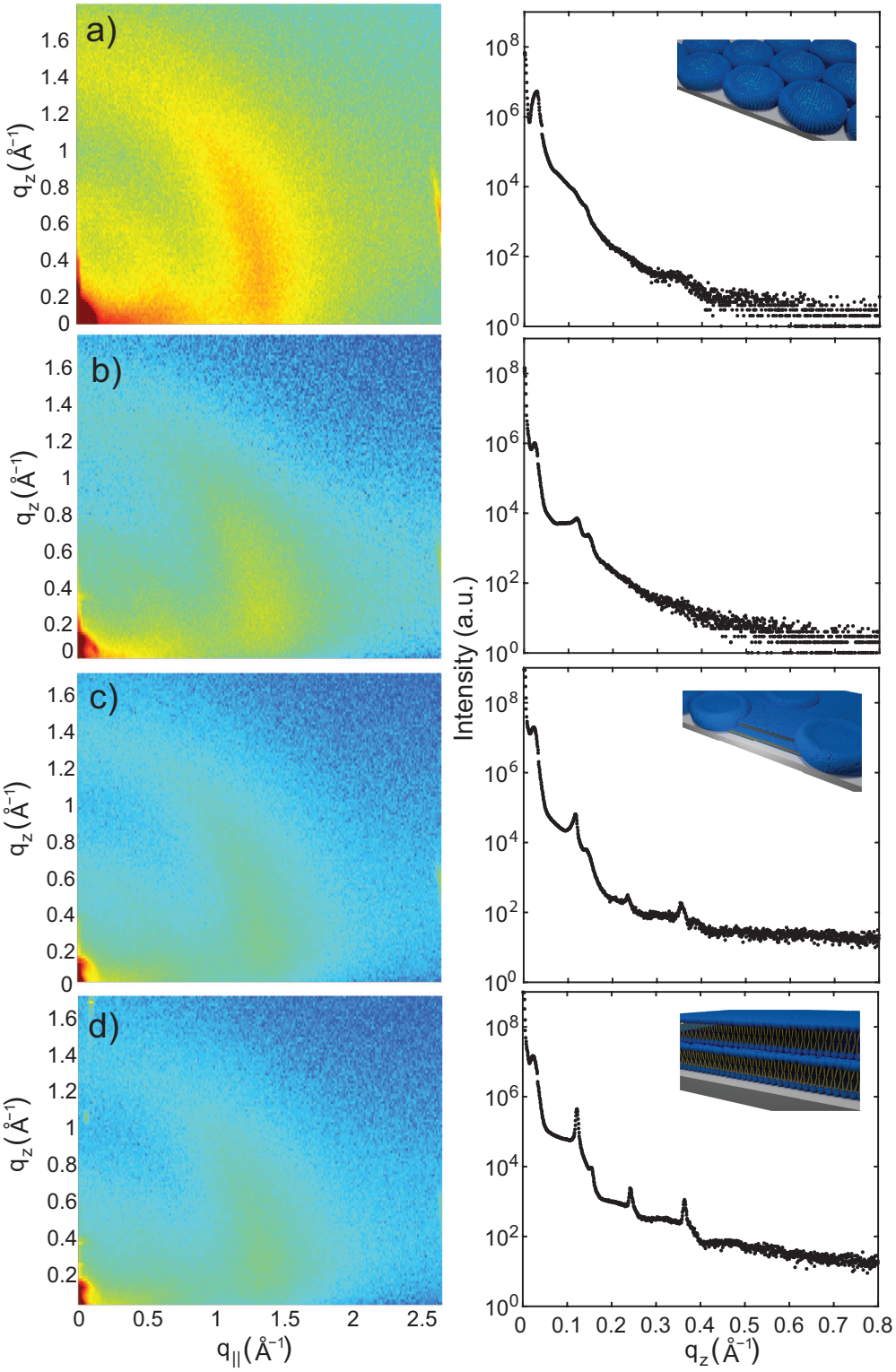

Figure 4.1.: 2D intensity map and the corresponding Bragg curve along the q_z-axis after a) application of the RBC solution on a hydrophilic wafer and fast drying, b) application on a hydrophobic wafer after slow drying. c) and d) show hydrophilic wafers after slow drying and slow drying and annealing, respectively. See text for details.

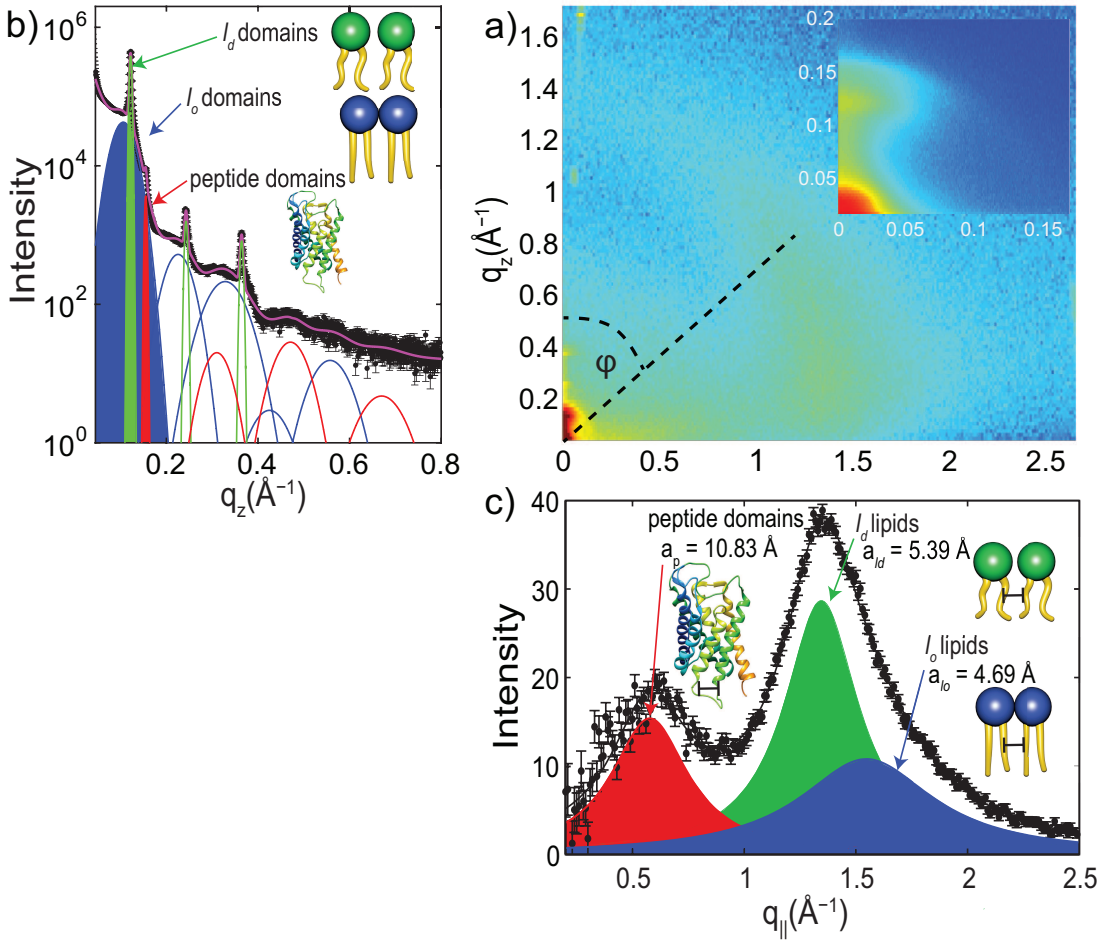

Figure 4.2.: Overview of the X-ray diffraction results. The highly aligned membranes are oriented on the X-ray diffractometer, such that q_z measures out-of-plane, and $q_{||}$ in-plane membrane structure. b) Two-dimensional data. The main features are a series of intensities along the q_z-axis and three broad signals along the in-plane axis $q_{||}$. a) shows a cut along q_z. The data are well fit by three series of Bragg peaks corresponding to three different lamellar spacings assigned to l_o and l_d lipid domains (green and blue) and coiled-coil α-helical peptide domains (red). c) The in-plane signals show three correlation peaks corresponding to the packing of α-helices in the peptide domains ($a_p = 10.83$ Å), and packing distances of l_d ($a_{ld} = 5.39$ Å) and l_o lipid tails ($a_{lo} = 4.69$ Å) in the hydrophobic membrane core. (Figure from [1])

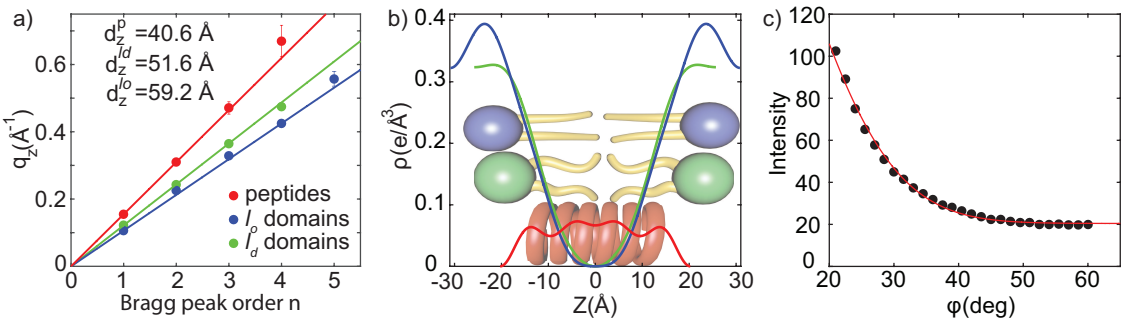

Figure 4.3.: Analysis of the X-ray diffraction data in Fig. 4.2. The lamellar spacings of the peptide, and the l_o and l_d lipid domains are determined from the slopes of q_z *vs.* n plots. b) Shows the corresponding electron densities, as determined through Fourier analysis of the out-of-plane diffraction data. The densities for the l_o and l_d lipid domains agree well with densities reported in the literature. The peptide domain shows an almost constant density in the hydrophobic membrane core, indicative of trans-membrane peptides. c) Membrane orientation is determined from radial integration of the scattered intensity along the meridional degree, φ. The solid line is a fit using a Gaussian profile. By using Hermans orientation function, RBC membranes are 90.9% oriented with respect to the silicon substrate. (Figure from from [1]).

assigned to three different structures: liquid ordered (l_o) and liquid disordered (l_d) lipid domains, and membrane embedded peptides [1], as will be detailed in Chap. 5.

Structure Perpendicular to the Membrane Plane

The well developed Bragg peaks along the out-of-plane axis in Fig. 4.2 c) are indicative of a lamellar organization of the RBC membranes on the substrate. The fundamental reflection for each series is colored in the Figure. Following Bragg's law (see Eq. 1.2), the lamellar spacing, d_z, can be determined from the slope of the curve when plotting q_z versus the order of the Bragg peak, n. This is shown in Fig. 4.3 a). Three d_z-spacings were determined: d_z^{lo}=59.2 Å, d_z^{ld}=51.6 Å and d_z^{p}=40.6 Å.

Electron density profiles, $\rho(z)$, of the bilayers were determined through Fourier analysis of the out-of-plane Bragg peaks, as described in Chap. 1.1.2, and are shown in Fig. 4.3 b). The electron rich head group can be identified by the absolute maximum in the electron density profile at $|z| \sim 22$ Å. ρ monotonically decreases towards the bilayer center at $z = 0$, where CH_3 groups typically reside, with a low electron density. The electron density profile of the d_z^{lo}=59.2 Å domain (blue

	l_o lipid domains	l_d lipid domains	peptide domains
d_z	59.2±0.5 Å	51.6±0.02 Å	40.6±0.06 Å
d_{HH}	46.0±0.5 Å	41.0±0.02 Å	-
d_w	13.2±0.5 Å	10.6±0.02 Å	-
a	4.69±0.27 Å	5.39±0.03 Å	10.88±0.22 Å
A_T	19.04±1.10 Å	25.18±0.13 Å	-
ξ	16±3 Å	29±2 Å	28±3 Å

Table 4.1.: The lamellar d_z spacings, molecular distances, a, and tail areas, A_T, were determined from the peak positions in the out-of-plane and in-plane scattering, respectively. Tail areas include the area of cholesterol molecules. Membrane thickness, d_{HH}, and the thickness of the water layer, d_w, were determined from the electron densities $\rho(z)$. Domain sizes, ξ, were determined from the width of the in-plane correlation peaks. Experimental errors are given.(Table from [1])

curve) agrees well with a lipid bilayer with lipids in the gel state with their lipid chains in an all-trans configuration [4, 20]. Together with the information from the in-plane diffraction below, these signals were assigned to lipids in l_o domains. These domains are likely enriched in cholesterol, making them more ordered and thicker [25, 30].

The electron density corresponding to the d_z^{ld}=51.6 Å spacing (green curve) agrees well with the electron density reported for fluid lipid bilayers, where the structure of the lipid tails in the hydrophobic membrane core is dominated by gauche-defects, as reported for instance by [27, 85]. Taking into account the in-plane diffraction analysis, these signals were assigned to domains of l_d lipids.

The 3^{rd} lamellar spacing of d_z^p=40.6 Å is significantly smaller than the spacings above, and the electron density is almost constant in the hydrophobic membrane core. This density profile is well described by α-helical coiled-coil peptides, which are embedded in the membranes [31], as will be discussed below, and was assigned to domains of integral proteins.

Lamellar spacings, d_z, membrane thicknesses, d_{HH}, and the thicknesses of the water layer, d_w were determined from the electron densities and are listed in Table 4.1[1].

In-Plane Membrane Structure

Three peaks, at $q_{\|} = 0.58$ Å^{-1}, $q_{\|} = 1.35$ Å^{-1} and $q_{\|} = 1.55$ Å^{-1}, were observed in the in-plane diffraction in Fig. 4.2 d). These peaks fit well to distances between peptides and lipids, as observed in previous investigations in single and multi-component artificial and biological membranes [26, 27, 28, 29, 30, 31]. The lipid in-plane peaks are the result of a hexagonal packing of the lipid tails in the hydrophobic membrane core (planar group p6) [25]. The distance between two acyl tails is determined to be $a = 4\pi/(\sqrt{3}q_{\|})$, where $q_{\|}$ is the position of the corresponding correlation peak. The area per lipid chain is obtained to $A_T = (\sqrt{3}/2)\ a^2$. This area also includes the area of cholesterol molecules.

The peaks at $q_{\|} = 1.35$ Å^{-1} and $q_{\|} = 1.55$ Å^{-1} are in good agreement with structural features reported in model lipid membranes in their well ordered gel and fluid phases, where the lipids tails take an all-trans conformation (gel) or are dominated by gauche defects (fluid). A correlation peak at ~1.5 Å^{-1} was reported in the gel phase of saturated phospholipid membranes, such as DMPC (Dimyristoyl-sn-glycero-3-phosphocholine) and DPPC (Dipalmitoyl-sn-glycero-3-phosphocholine) [20, 25, 26, 86]. Unsaturated lipids were reported to order in a structure with slightly larger nearest neighbor tail distances, leading to an acyl-chain correlation peak at ~1.3 Å^{-1}, as reported for DOPC and POPC [87, 88]. These correlation peaks were, therefore, assigned to the l_o and l_d lipid components of the plasma membranes.

Lipid tail distances in l_o and l_d domains and lipid tail areas are listed in Table 4.1. Distances and areas in the l_o domains are smaller, as lipid tails in their all-trans configuration are straighter and pack tighter than l_d tails, dominated by gauche defects.

Membrane peptides are often organized in bundles, whose structure is dominated by α-helical coiled-coils [31, 89, 90, 91, 92]. Coiled coils consist of α-helices wound together to form a ropelike structure stabilized by hydrophobic interactions, found in about 10% of the proteins in the human genome [93]. The main features of this motif is a ~10.8 Å ($q_{\|}$ ~0.58 Å^{-1}) equatorial reflection corresponding to the spacing between adjacent coiled-coils [94, 95, 96]. This correlation peak is observed in the in-plane data in Fig. 4.2 d) (in red).

The volume fractions of the peptide, the l_o and l_d lipid domains were determined from the integrated peak intensities of the lipid and peptide signals in Fig. 4.2 d) to 30:45:25 (l_o lipids:l_d lipids:coiled peptides) [1].

Membrane Orientation

The orientation of the RBC membranes in the stack with respect to the silicon wafer was determined from the 2-dimensional data in Fig. 4.2 b) by radial integration using Hermans orientation function, as described in Chap. 1.1.2. The intensity of the first reflectivity peak as function of the meridional angle φ is plotted in Fig. 4.3 c), and the degree of orientation was determined to be 90.9% (±0.26%). While values of ~97% are reported for synthetic supported membranes (see, *e.g.* [18]), the value for RBC membranes is to the best of our knowledge the highest ever reported for a biological membrane. This high degree of orientation of the RBC membranes on silicon chips is required for a detailed structural characterization of the membranes, in particular to differentiate in-plane and out-of-plane structure [1].

Determination of Domain Size

The in-plane diffraction signals in Fig. 4.2 d) are significantly broader than typical Bragg peaks in crystalline materials, indicating that the corresponding domains are small. The domain sizes were estimated from the peak widths of the corresponding correlation peaks using Scherrer's equation (see Eq. 1.24). Values for the domain size, ξ, are listed in Table 4.1. From these results, RBC membranes consist of small, nanometer sized domains of l_o and l_d lipids and coiled-coil α-helical peptides [1].

4.2. The Effect of Aspirin on Red Blood Cell Membrane Structure

The out-of-plane scattering for RBC membranes containing 1 mM, 1.5 mM, 2 mM, 2.5 mM and 3 mM ASA is shown in Fig. 4.4 a). The curve containing 2.5 mM ASA and the corresponding fit is shown in part b). Data is well fit by 3 series of Bragg peaks, corresponding to l_o, l_d and peptide domains, in agreement with pure RBC membranes. Electron density profiles of the l_o lipid domain for RBC membranes and RBC membranes + 1mM aspirin are shown in Fig. 4.4 c). Upon the addition of aspirin, the electron density increases at $z \sim 22.8$ Å. Under the assumption that a small amount of aspirin does not disturb the bilayer structure significantly, the two densities can be subtracted and the extra intensity assigned to aspirin molecules. The experiments thus locate aspirin inside the head group

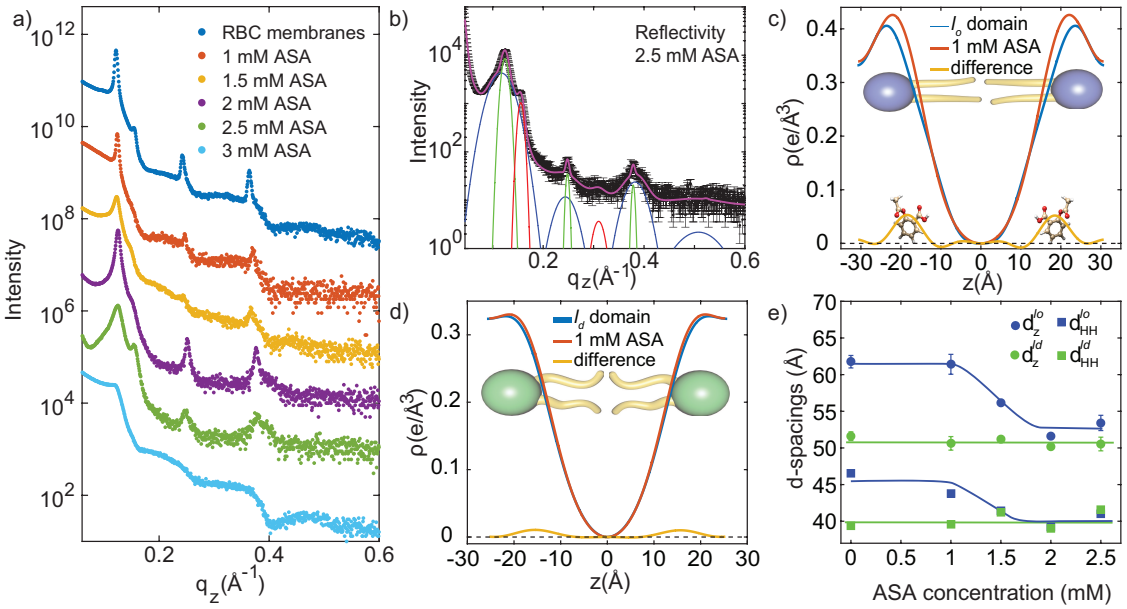

Figure 4.4.: Analysis of the RBC/aspirin complexes. a) Shows all reflectivity curves for complexes containing between 0 and 3 mM ASA. b) The pattern for the 2.5 mM sample is well fit by three series of peaks corresponding to l_o, l_d and peptide domains. c) The location of the ASA molecule is determined by comparing the electron density of a pure RBC membrane with a low concentration of 1 mM ASA. Aspirin is found to partition the l_o lipid domains of RBC membranes and locate in the head group region, at $|z|$-values of 22.8 Å. d) Small partitioning of aspirin is observed in l_d lipid domains, indicative that aspirin preferably interacts with l_o domains. e) Lamellar spacing, d_z, and membrane thickness, d_{HH}, of the l_o lipid domains decrease significantly with increasing ASA concentration until thickness of l_o and l_d domains coincide. Due to the absence of reflectivity peaks in the 3 mM ASA curve in part a) no d-spacings could be determined for this concentration in part e). (Figure from [1]).

region of the RBC membranes, in agreement with results in model phospholipid bilayers [3, 4, 19]. There is only a small effect of aspirin on the electron density of the l_d domains, as shown in Fig. 4.4 d), indicating that aspirin preferably interacts with l_o regions.

The lamellar spacing, d_z and head group to head group spacing, d_{HH}, of the l_o and l_d lipid domains as function of ASA content are depicted in Fig. 4.4 e). While lamellar spacing and membrane thickness for the l_d lipid domains are not affected by the presence of ASA, the two spacings significantly decrease with increasing aspirin concentrations for the l_o lipid domains. They decrease until lamellar spacing and membrane thickness for l_o and l_d domains coincide at a ASA concentration of 2.5 mM. At this ASA concentration, the overall lamellar spacing of the RBC membranes is reduced to 53.4 Å; the overall membrane thickness to 41.8 Å[1].

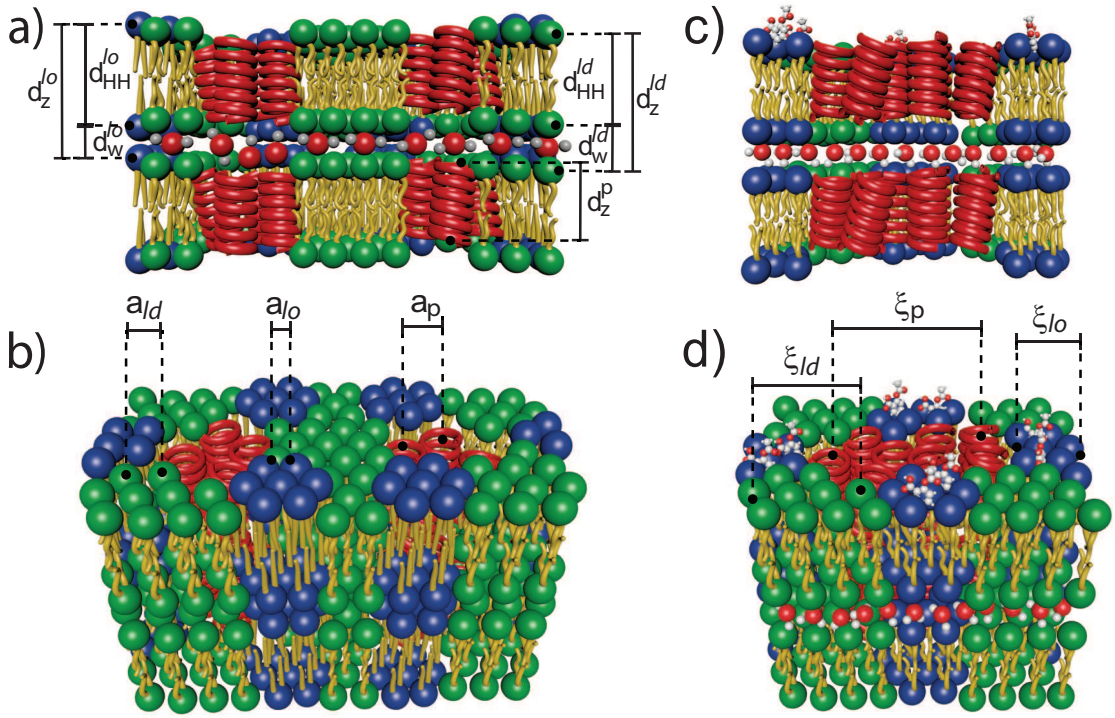

Figure 4.5.: The structural findings are summarized in cartoons of pure RBC membranes in a) and b), and RBC membranes containing aspirin in c) and d). The images show side and top views. Structural parameters, such as the lamellar spacing, d_z, the head group to head group thickness of the membranes, d_{HH}, the thickness of the water layer, d_w, and in-plane distances between lipid tails and integral peptides, a, and domain sizes, ξ, were determined for the l_o and l_d lipid, and the peptide domains. While the l_o and l_d lipid domains showed significantly different membrane thicknesses in pure RBC membranes, the addition of aspirin led to an overall thinning of the membranes and an increase of the lipid spacings, indicative of a fluidification. Aspirin was found to interact mainly with the l_o lipid domains. (Figure from [1]).

5. Discussion

In order to efficiently use biophysical techniques, such as fluorescence microscopy, atomic force microscopy, as well as X-ray and neutron scattering, highly oriented stacks of supported lipid bilayers are usually prepared [97]. These techniques are ideally suited to study molecular structure and dynamical properties of membranes [17, 47, 98, 99, 100, 101, 102, 103, 104, 105]. The approach has advanced significantly during the past decades and is now used to study complex, multi-component membranes and their interaction with drugs, small molecules [2, 3, 8, 17, 31, 48, 88, 106, 107, 108, 109], bacteria [110, 111], and in particular lipid rafts, *i.e.* functional lipid domains [25, 30, 51, 52, 53, 54, 55]. The preparation protocol presented in this thesis produces highly oriented, multi-lamellar RBC membranes on silicon wafers, which are highly suited to provide detailed molecular level information. The combination of oriented membranes and state-of-the-art diffraction equipment and analysis gives unprecedented insight into the structure of these RBC membranes [1].

In early X-ray diffraction studies of human erythrocytes membranes [46, 112, 113] ghosts were prepared using the Dodge protocol and pellets of the final preparation were imaged. Diffraction patterns with lamellar periodicities between ~55 and ~70 Å were observed and assigned to hemoglobin free membranes, in agreement with the presented findings. Large amounts of hemoglobin were reported to result in much larger lamellar periodicities of ~110 Å [112]. The electron density in Fig. 4.3 b) agrees qualitatively with the early electron density in [113], which was assigned to intact, hemoglobin-free erythrocyte membranes. However, the low purity and low degree of order in the RBC pellets likely prohibited a more detailed structural analysis at this time [1].

From X-ray diffraction along the membrane normal, the lamellar spacing, d_z, the membrane thickness, d_{HH} and the thickness of the water layer, d_w, were determined and are listed in Table 4.1. From in-plane diffraction data, molecular distances and areas were determined. The out-of-plane and in-plane data in particular present

evidence for a patchy structure: these RBC membranes consist of nanometer-sized liquid ordered (l_o) and liquid disordered (l_d) lipid domains and α-helical coiled-coil peptide domains (integral proteins), at ratios of 30.2% l_o, 45.0% l_d and 24.8% coiled peptides. By assigning the scattering signals to the different phases, one can determine structural parameters for these domains separately. The structure of the multi-lamellar, solid supported RBC membranes is pictured in Figs. 4.5 a) and b) [1].

The structure of RBC membranes is no longer thought to be uniform, but to show 'rafts', regions enriched in cholesterol and sphingolipids in association with specific membrane proteins [68]. Rafts are typically thought to be a manifestation of the liquid ordered phase and, as such, enriched in cholesterol, thicker and with lipids showing gel-like properties. In nonerythroid cells, lipid rafts are suspected to be relevant for cell signaling events. In erythroid cells, they have been shown to mediate β2-adregenic receptor signaling and increase cAMP levels, and thus regulating entry of malarial parasites into normal red cells [114]. Properties and even existence of rafts are, however, a topic of intense debate in the literature [52, 54, 55]. The reason is that the data indicate rafts as very small and highly dynamics structures, which are very difficult to observe. It is challenging for experimental techniques to cover the small length scales and fast dynamics at the same time [1].

Heterogeneities have indeed been observed in human erythrocytes. The main technique used is detergent-resistant-membranes (DRM), a membrane fraction resisting solubilization by a detergent [56]. Recently, raft-like heterogeneities have also been reported from fluourescent labeling techniques in live erythrocytes [56, 57]. The structures observed in this paper are in very good agreement with the raft hypothesis: they are small, nanometer-sized patches and the lipids in one of the patches appear indeed to be more gel-like and the corresponding patches to be thicker. They, therefore, have been labeled as liquid ordered phase. While diffraction can be sensitive to small fluctuating membrane structures [25, 30], the structures observed here likely show a slower dynamics. It can be speculated that the presence of a solid support possibly leads to changes in the raft dynamics of the RBC membranes on a chip, as compared to the membrane in intact red blood cells [1].

The structural parameters of the three different membrane patches in Table 4.1 are in excellent agreement with values reported from model membrane studies. The two lipid domains were interpreted as manifestations of liquid ordered and liquid disordered phases. The l_o domains were found to be thicker (d_{HH}= 46 Å),

with a relatively small area per lipid tail of A_T=19 Å^2, while the l_d domains are significantly thinner (41 Å) with a greater lipid tail area (A_T=25 Å^2), typical for a fluid structure. The average thickness of the peptide domains of 40.6 Å is compatible with the thickness of the membranes and support the assignment to integral peptides. The corresponding patch sizes are small, between about 20 and 30 Å.

While RBC membranes were previously reported to consist of ~52% proteins and ~40% lipids (including cholesterol) [69], a higher fraction of lipids (and cholesterol) and fewer peptides were observed. The X-ray diffraction used is not sensitive to monomeric integral or peripheral peptides, but to larger integral peptide regions (the packing of peptide helices in the membrane core). These helical regions are likely part of larger trans-membrane proteins. Chemical analysis techniques or mass spectrometry may, therefore, result in a higher total concentration of peptides. The value determined in this work indicates that about 50% of the peptides in RBC membranes can be considered as integral membrane proteins.

There is growing evidence for an influence of various pharmaceuticals on lipid membrane organization and stability [72]. In particular, non-steroidal anti-inflammatory drugs (NSAID's) have been shown to disturb bilayer structures in native and model membranes [7, 73]. Aspirin is the most common NSAID and is known to interact with membranes [4, 73]. Aspirin strongly perturbs model membrane structure in a concentration dependent manner and also influences human erythrocyte shape [76]. It decreases the hydrophobic surface barrier in mucosal membranes, leading to a diffusion of acid and gastrointestinal injury [6] and impacts on protein sorting [77]. Aspirin was previously reported to partition in lipid bilayers and position itself in the lipid head group region [3, 4, 19]. Recently, an interaction between aspirin and cholesterol was reported, as aspirin was observed to reduce the volume of cholesterol plaques in model membranes at elevated cholesterol concentrations of ~40 mol% [19]. Aspirin also inhibits the formation of cholesterol rafts in fluid lipid membranes at physiological cholesterol concentrations [3, 19] [1].

The effect of ASA on the molecular organization of RBC was determined by X-ray diffraction. The main findings are that aspirin partitions in RBC membranes, and is located in the membrane head group region. Aspirin was found to reduce membrane thickness and increases lipid tail distances, indicative of a fluidification of the RBC membranes. This observation is in excellent agreement with the findings in model membranes. A cartoon of the structure of RBC membranes in the presence of ASA

is shown in Figs. 4.5 c) and d).
An interesting point is that aspirin was preferably found in the l_o lipid regions of the RBC membranes. By calculating electron densities for the l_d and l_o domains in Fig. 4.4 c) and d), a significant difference was observed for the l_o domains, only. This led to a thinning of the l_o domains and an increase in area per lipid tail, indicative of a fluidification of these more densely organized regions of the RBC membranes. This is in excellent agreement with observation in model membranes, where a strong interaction between model membranes in liquid ordered phases and aspirin was reported [3, 4, 19]. Also in model membranes, ASA was found to locate in the head group region of the bilayers and make bilayers more fluid and dissolve cholesterol structures, such as plaques and rafts [1].
ASA has a pronounced effect on the RBC membranes in this study: by reducing the thickness of the l_o regions it leads to a more uniform and overall more fluid membrane structure, where the l_d and l_o domains now have identical membrane thicknesses. This finding suggests aspirin exerts an effect on the physical properties of red-blood cell membranes, which may in turn help to understand the side-effects of aspirin and the low-dose-aspirin therapy [1].
The presented results demonstrate, that these RBC on a chip can be used as a platform to test the interaction of other drugs and bacteria with RBC membranes and determine their molecular mode-of-action in the future.

A. Appendix A

A.1. Copyright Information for Images and Publications

A.1.1. Scientific Report Publication [1]

Excerpt from `https://www.nature.com/articles/srep39661` [Online; accessed 26-May-2017] regarding the reproduction of this article:
"This work is licensed under a Creative Commons Attribution 4.0 International License. The images or other third party material in this article are included in the article's Creative Commons license, unless indicated otherwise in the credit line; if the material is not included under the Creative Commons license, users will need to obtain permission from the license holder to reproduce the material."

A.1.2. Figure 2.4

Excerpt from `https://commons.wikimedia.org/wiki/File:RBC_Membrane_Proteins_SDS-PAGE_gel.jpg` [Online; accessed 26-May-2017] regarding the reproduction of this figure:
"This work is free and may be used by anyone for any purpose. If you wish to use this content, you do not need to request permission as long as you follow any licensing requirements mentioned on this page."

A.1.3. Figure 1.1

The licence agreement below details between myself and Springer that show and terms of reproduction of Figure 10.1 from [8] for use in this thesis.

SPRINGER LICENSE
TERMS AND CONDITIONS

May 26, 2017

This Agreement between Saarland University -- Sebastian Himbert ("You") and Springer ("Springer") consists of your license details and the terms and conditions provided by Springer and Copyright Clearance Center.

License Number	4114660343475
License date	May 23, 2017
Licensed Content Publisher	Springer
Licensed Content Publication	Springer eBook
Licensed Content Title	Lipid Membrane Dynamics
Licensed Content Author	Maikel C. Rheinstädter
Licensed Content Date	Jan 1, 2012
Type of Use	Thesis/Dissertation
Portion	Figures/tables/illustrations
Number of figures/tables /illustrations	1
Author of this Springer article	No
Order reference number	
Original figure numbers	figure 10.1
Title of your thesis / dissertation	The Molecular Structure of Human Red Blood Cell Membranes from Highly Oriented, Solid Supported Multi-Lamellar Membranes
Expected completion date	May 2017
Estimated size(pages)	80
Requestor Location	Saarland University Campus, building E2 6 Post office box 15 11 50 Saarbrücken, Saarland 66123 Germany Attn: Saarland University
Billing Type	Invoice
Billing Address	Saarland University Campus, building E2 6 Post office box 15 11 50 Saarbrücken, Germany 66123 Attn: Saarland University
Total	**0.00 EUR**
Terms and Conditions	

Introduction

The publisher for this copyrighted material is Springer. By clicking "accept" in connection with completing this licensing transaction, you agree that the following terms and conditions apply to this transaction (along with the Billing and Payment terms and conditions established by Copyright Clearance Center, Inc. ("CCC"), at the time that you opened your Rightslink account and that are available at any time at http://myaccount.copyright.com).

Limited License

With reference to your request to reuse material on which Springer controls the copyright, permission is granted for the use indicated in your enquiry under the following conditions:

- Licenses are for one-time use only with a maximum distribution equal to the number stated in your request.

- Springer material represents original material which does not carry references to other sources. If the material in question appears with a credit to another source, this permission is not valid and authorization has to be obtained from the original copyright holder.
- This permission
• is non-exclusive
• is only valid if no personal rights, trademarks, or competitive products are infringed.
• explicitly excludes the right for derivatives.
- Springer does not supply original artwork or content.
- According to the format which you have selected, the following conditions apply accordingly:
• **Print and Electronic:** This License include use in electronic form provided it is password protected, on intranet, or CD-Rom/DVD or E-book/E-journal. It may not be republished in electronic open access.
• **Print:** This License excludes use in electronic form.
• **Electronic:** This License only pertains to use in electronic form provided it is password protected, on intranet, or CD-Rom/DVD or E-book/E-journal. It may not be republished in electronic open access.
For any electronic use not mentioned, please contact Springer at permissions.springer@spi-global.com.
- Although Springer controls the copyright to the material and is entitled to negotiate on rights, this license is only valid subject to courtesy information to the author (address is given in the article/chapter).
- If you are an STM Signatory or your work will be published by an STM Signatory and you are requesting to reuse figures/tables/illustrations or single text extracts, permission is granted according to STM Permissions Guidelines: http://www.stm-assoc.org/permissions-guidelines/
For any electronic use not mentioned in the Guidelines, please contact Springer at permissions.springer@spi-global.com. If you request to reuse more content than stipulated in the STM Permissions Guidelines, you will be charged a permission fee for the excess content.
Permission is valid upon payment of the fee as indicated in the licensing process. If permission is granted free of charge on this occasion, that does not prejudice any rights we might have to charge for reproduction of our copyrighted material in the future.
-If your request is for reuse in a Thesis, permission is granted free of charge under the following conditions:
This license is valid for one-time use only for the purpose of defending your thesis and with a maximum of 100 extra copies in paper. If the thesis is going to be published, permission needs to be reobtained.
- includes use in an electronic form, provided it is an author-created version of the thesis on his/her own website and his/her university's repository, including UMI (according to the definition on the Sherpa website: http://www.sherpa.ac.uk/romeo/);
- is subject to courtesy information to the co-author or corresponding author.
Geographic Rights: Scope
Licenses may be exercised anywhere in the world.
Altering/Modifying Material: Not Permitted
Figures, tables, and illustrations may be altered minimally to serve your work. You may not alter or modify text in any manner. Abbreviations, additions, deletions and/or any other alterations shall be made only with prior written authorization of the author(s).
Reservation of Rights
Springer reserves all rights not specifically granted in the combination of (i) the license details provided by you and accepted in the course of this licensing transaction and (ii) these terms and conditions and (iii) CCC's Billing and Payment terms and conditions.
License Contingent on Payment
While you may exercise the rights licensed immediately upon issuance of the license at the end of the licensing process for the transaction, provided that you have disclosed complete and accurate details of your proposed use, no license is finally effective unless and until full payment is received from you (either by Springer or by CCC) as provided in CCC's Billing and Payment terms and conditions. If full payment is not received by the date due, then any license preliminarily granted shall be deemed automatically revoked and shall be void as if never granted. Further, in the event that you breach any of these terms and conditions or any of CCC's Billing and Payment terms and conditions, the license is automatically revoked and shall be void as if never granted. Use of materials as described in a revoked license, as well as any use of the materials beyond the scope of an unrevoked license, may constitute copyright infringement and Springer reserves the right to take any and all action to protect its copyright in the materials.
Copyright Notice: Disclaimer
You must include the following copyright and permission notice in connection with any reproduction of the licensed material: "Springer book/journal title, chapter/article title, volume, year of publication, page, name(s) of author(s), (original copyright notice as given in the publication in which the material was originally published) "With permission of Springer"
In case of use of a graph or illustration, the caption of the graph or illustration must be included, as it is indicated in the original publication.
Warranties: None
Springer makes no representations or warranties with respect to the licensed material and adopts on its own behalf the limitations and disclaimers established by CCC on its behalf in its Billing and Payment terms and conditions for this licensing transaction.
Indemnity

You hereby indemnify and agree to hold harmless Springer and CCC, and their respective officers, directors, employees and agents, from and against any and all claims arising out of your use of the licensed material other than as specifically authorized pursuant to this license.

No Transfer of License

This license is personal to you and may not be sublicensed, assigned, or transferred by you without Springer's written permission.

No Amendment Except in Writing

This license may not be amended except in a writing signed by both parties (or, in the case of Springer, by CCC on Springer's behalf).

Objection to Contrary Terms

Springer hereby objects to any terms contained in any purchase order, acknowledgment, check endorsement or other writing prepared by you, which terms are inconsistent with these terms and conditions or CCC's Billing and Payment terms and conditions. These terms and conditions, together with CCC's Billing and Payment terms and conditions (which are incorporated herein), comprise the entire agreement between you and Springer (and CCC) concerning this licensing transaction. In the event of any conflict between your obligations established by these terms and conditions and those established by CCC's Billing and Payment terms and conditions, these terms and conditions shall control.

Jurisdiction

All disputes that may arise in connection with this present License, or the breach thereof, shall be settled exclusively by arbitration, to be held in the Federal Republic of Germany, in accordance with German law.

Other conditions:

V 12AUG2015

Questions? customercare@copyright.com or +1-855-239-3415 (toll free in the US) or +1-978-646-2777.

Bibliography

[1] Sebastian Himbert, Richard J. Alsop, Markus Rose, Laura Hertz, Alexander Dhaliwal, Jose M. Moran-Mirabal, Chris P. Verschoor, Dawn M. E. Bowdish, Lars Kaestner, Christian Wagner, and Maikel C. Rheinstädter. The molecular structure of human red blood cell membranes from highly oriented, solid supported multi-lamellar membranes. Scientific Reports, 7:39661, jan 2017.

[2] Richard J Alsop, Clare L Armstrong, Amna Maqbool, Laura Toppozini, Hannah Dies, and Maikel C Rheinstädter. Cholesterol expels ibuprofen from the hydrophobic membrane core and stabilizes lamellar phases in lipid membranes containing ibuprofen. Soft matter, 11(24):4756–4767, 2015.

[3] Richard J Alsop, Laura Toppozini, Drew Marquardt, Norbert Kučerka, Thad A Harroun, and Maikel C Rheinstädter. Aspirin inhibits formation of cholesterol rafts in fluid lipid membranes. Biochimica et Biophysica Acta (BBA)-Biomembranes, 1848(3):805–812, 2015.

[4] Matthew A. Barrett, Songbo Zheng, Golnaz Roshankar, Richard J. Alsop, Randy K.R. Belanger, Chris Huynh, Norbert Kučerka, and Maikel C. Rheinstädter. Interaction of aspirin (acetylsalicylic acid) with lipid membranes. PLoS ONE, 7(4):e34357, 04 2012.

[5] James T Dodge, Carolyn Mitchell, and Donald J Hanahan. The preparation and chemical characteristics of hemoglobin-free ghosts of human erythrocytes. Archives of biochemistry and biophysics, 100(1):119–130, 1963.

[6] Lenard M Lichtenberger, Yong Zhou, Elizabeth J Dial, and Robert M Raphael. Nsaid injury to the gastrointestinal tract: evidence that nsaids interact with phospholipids to weaken the hydrophobic surface barrier and induce the formation of unstable pores in membranes. J. Pharm. Pharmacol., 58(11):1421–1428, 2006.

[7] Catarina Pereira-Leite, Cláudia Nunes, and Salette Reis. Interaction of non-steroidal anti-inflammatory drugs with membranes: In vitro assessment and relevance for their biological actions. Progress in lipid research, 52(4):571–584, 2013.

[8] Maikel C. Rheinstädter. Lipid membrane dynamics. In Victoria García Sakai, Christiane Alba-Simionesco, and Sow-Hsin Chen, editors, Dynamics of Soft Matter: Neutron Applications, pages 263–286. Springer-Verlag GmbH, 2011. ISBN 978-1-4614-0726-3.

[9] A. Einstein. Über einen die erzeugung und verwandlung des lichtes betreffenden heuristischen gesichtspunkt. Annalen der Physik, 322(6):132–148, 1905.

[10] L. de Brogli. The light quantum. Phil. Mag, 47(446), 1924.

[11] J. Keppler. Strena seu de Nive Sexangula. Frankfurt: G. Tampach, 1611.

[12] Friedrich W., Knipping P, and von Laue M. Interferenz-erscheinungen bei röntgenstrahlen. Sitzungsberichte der Mathematisch-Physikalischen Classe der Königlich-Bayerischen Akademie der Wissenschaften zu München, 303, 1912.

[13] M. von Laue. Die interferenzerscheinungen an röntgenstrahlen, hervorgerufen durch das raumgitter der kristalle. Jahrbuch der Radioaktivität und Elektronik, 11(3):308 – 345, 1914.

[14] W.L. Bragg. Die reflexion der röntgenstrahlen. Jahrbuch der Radioaktivität und Elektronik, 11(3):346 – 391, 1914.

[15] W. L. Bragg. The structure of some crystals as indicated by their diffraction of x-rays. Proceedings of the Royal Society of London A: Mathematical, Physical and Engineering Sciences, 89(610):248–277, 1913.

[16] R. Gross and A. Marx. Festkörperphysik. Oldenbourg Wissensch.Vlg, 2012. ISBN 978-3-486-71294-0.

[17] G. Pabst, N. Kučerka, M.-P. Nieh, M.C. Rheinstädter, and J. Katsaras. Applications of neutron and x-ray scattering to the study of biologically relevant model membranes. Chemistry and Physics of Lipids, 163(6):460 – 479, 2010.

[18] Richard J Alsop, Rafaëla Schober, and Maikel Christian Rheinstadter. Swelling of phospholipid membranes by divalent metal ions depends on the location of the ions in the bilayers. Soft Matter, 2016.

[19] Richard J Alsop, Matthew A Barrett, Songbo Zheng, Hannah Dies, and Maikel C Rheinstädter. Acetylsalicylic acid (asa) increases the solubility of cholesterol when incorporated in lipid membranes. Soft matter, 10(24):4275–4286, 2014.

[20] Stephanie Tristram-Nagle, Yufeng Liu, Justin Legleiter, and John F. Nagle. Structure of gel phase dmpc determined by x-ray diffraction. Biophysical Journal, 83:3324–3335, 2002.

[21] J. F. Nagle and M. C. Wiener. Relations for lipid bilayers. Biophys. J., 55 (55):309–313, 1989.

[22] J.F. Nagle, R. Zhang, S. Tristram-Nagle, W. Sun, H.I. Petrache, and R.M. Suter. X-ray structure determination of fully hydrated lα phase dipalmitoylphosphatidylcholine bilayers. Biophys. J., 70:1419–1431, 1996.

[23] P. Scherrer. Bestimmung der Größe und der inneren Struktur von Kollidteilchen mittels Röntgenstrahlen. Göttinger Nachrichten Math. Phys., 2: 98–100, 1918.

[24] J. I. Langford and A. J. C. Wilson. Scherrer after sixty years: A survey and some new results in the determination of crystallite size. Journal logo Journal of Applied Crystallography, 11(2):102–113, 1978.

[25] Clare L. Armstrong, Drew Marquardt, Hannah Dies, Norbert Kučerka, Zahra Yamani, Thad A. Harroun, John Katsaras, An-Chang Shi, and Maikel C. Rheinstädter. The observation of highly ordered domains in membranes with cholesterol. PLOS ONE, 8:e66162, 2013.

[26] M. C. Rheinstädter, C. Ollinger, G. Fragneto, F. Demmel, and T. Salditt. Collective dynamics of lipid membranes studied by inelastic neutron scattering. Phys. Rev. Lett., 93:108107, 2004.

[27] Norbert Kučerka, Yufeng Liu, Nanjun Chu, Horia I. Petrache, Stephanie Tristram-Nagle, and John F. Nagle. Structure of fully hydrated fluid phase

DMPC and DLPC lipid bilayers using x-ray scattering from oriented multilamellar arrays and from unilamellar vesicles. Biophys. J., 88:2626–2637, 2005.

[28] R. Welti, D.A. Rintoul, F. Goodsaid-Zalduondo, S. Felder, and D.F. Silbert. Gel-phase phospholipid in the plasma membrane of sterol-depleted mouse lm cells. The Journal of Biological Chemistry, 256:7528–7535, 1981.

[29] Danny Poinapen, Laura Toppozini, Hannah Dies, Daniel CW Brown, and Maikel C Rheinstädter. Static magnetic fields enhance lipid order in native plant plasma membrane. Soft Matter, 9(29):6804–6813, 2013.

[30] Laura Toppozini, Sebastian Meinhardt, Clare L Armstrong, Zahra Yamani, Norbert Kučerka, Friederike Schmid, and Maikel C Rheinstädter. Structure of cholesterol in lipid rafts. Physical review letters, 113(22):228101, 2014.

[31] Jennifer Tang, Richard J Alsop, Matilda Backholm, Hannah Dies, An-Chang Shi, and Maikel C Rheinstädter. Amyloid-β 25–35 peptides aggregate into cross-β sheets in unsaturated anionic lipid membranes at high peptide concentrations. Soft matter, 12(13):3165–3176, 2016.

[32] microscopyu.com. The diffraction barrier in optical microscopy. https://www.microscopyu.com/techniques/super-resolution/the-diffraction-barrier-in-optical-microscopy, 2017. [Online; accessed 03-May-2017].

[33] microscopyu.com. Numerical aperture. `https://www.microscopyu.com/microscopy-basics/numerical-aperture`, 2017. [Online; accessed 30-January-2017].

[34] ThermoFisher. Fluorescence spectraviewer. `https://www.thermofisher.com/de/de/home/life-science/cell-analysis/labeling-chemistry/fluorescence-spectraviewer.html`, 2017. [Online; accessed 30-January-2017].

[35] ThermoFisher. Dii. `https://www.thermofisher.com/order/catalog/product/D282`, 2017. [Online; accessed 30-January-2017].

[36] Wikipedia. Electromagnetic spectrum — Wikipedia, the free encyclopedia. `http://en.wikipedia.org/w/index.php?title=Electromagnetic%20spectrum&oldid=781454398`, 2017. [Online; accessed 23-May-2017].

[37] Paula Y. Bruice. Organische Chemie - Studieren kompakt. Pearson Deutschland GmbH, München, 5. edition, 2011. ISBN 978-3-868-94102-9.

[38] Photoelectric Spectrometry Group and Institut für Spektrochemie und Angewandte Spektroskopie. UV Atlas of Organic Compounds: UV Atlas Organischer Verbindungen. Number Bd. 2 in UV Atlas of Organic Compounds: UV Atlas Organischer Verbindungen. Plenum Press, 1966. ISBN 978-1-4757-6892-3.

[39] Matthias Brust, Othmane Aouane, Marine Thiébaud, Daniel Flormann, Claude Verdier, Lars Kaestner, MW Laschke, Hassib Selmi, Abdellilah Benyoussef, Thomas Podgorski, et al. The plasma protein fibrinogen stabilizes clusters of red blood cells in microcapillary flows. Scientific reports, 4, 2014.

[40] M Brust, C Schaefer, R Doerr, L Pan, M Garcia, PE Arratia, and C Wagner. Rheology of human blood plasma: Viscoelastic versus newtonian behavior. Physical review letters, 110(7):078305, 2013.

[41] Gerald Karp. Molekulare Zellbiologie (Springer-Lehrbuch) (German Edition), page 155ff. Springer Berlin Heidelberg, 2005. ISBN 3-540-23857-3.

[42] Daniel Flormann, Katharina Schirra, Thomas Podgorski, and Christian Wagner. On the rheology of red blood cell suspensions with different amounts of dextran: separating the effect of aggregation and increase in viscosity of the suspending phase. Rheologica Acta, 55(6):477–483, oct 2015.

[43] Eric M. Strohm, Elizabeth S.L. Berndl, and Michael C. Kolios. Probing red blood cell morphology using high-frequency photoacoustics. Biophysical Journal, 105(1):59–67, jul 2013.

[44] Lionel Bureau, Gwennou Coupier, Frank Dubois, Alain Duperray, Alexander Farutin, Christophe Minetti, Chaouqi Misbah, Thomas Podgorski, Daria Tsvirkun, and Mikhail Vysokikh. Blood flow and microgravity. Comptes Rendus Mécanique, 345(1):78–85, jan 2017.

[45] Werner A. Müller, Stephan Frings, and Frank Möhrlen. Tier- und Humanphysiologie, page 49ff. Springer Berlin Heidelberg, 2015. ISBN 978-3-662-43942-5.

[46] Leon McCaughan and S Krimm. X-ray and neutron scattering density profiles of the intact human red blood cell membrane. Science, 207(4438):1481–1483, 1980.

[47] J Daillant, E Bellet-Amalric, A Braslau, T Charitat, G Fragneto, F Graner, S Mora, F Rieutord, and B Stidder. Structure and fluctuations of a single floating lipid bilayer. Proceedings of the National Academy of Sciences of the United States of America, 102(33):11639–11644, 2005.

[48] Maikel C Rheinstädter. Basic aspects and applications of lipids and protein dynamics. In Norbert Kučerka, Georg Pabst, Mu-Ping Nieh, and John Katsaras, editors, Liposomes, Lipid Bilayers and Model Membranes: from Basic Research to Application, pages 111–124. CRC Press, 2014. ISBN 9781138198753.

[49] A. Stier and E. Sackmann. Spin labels as enzyme substrates heterogeneous lipid distribution in liver microsomal membranes. Biochimica et Biophysica Acta (BBA) - Biomembranes, 311(3):400–408, jul 1973.

[50] M. J. Karnovsky. The concept of lipid domains in membranes. The Journal of Cell Biology, 94(1):1–6, jul 1982.

[51] K. Simons and E. Ikonen. Functional rafts in cell membranes. Nature, 387: 569–572, 1997.

[52] Ka Simons and Mathias J. Gerl. Revitalizing membrane rafts: new tools and insights. Nat Rev Mol Cell Biol, 11(10):688–699, 2010.

[53] Sebastian Meinhardt, Richard L. C. Vink, and Friederike Schmid. Monolayer curvature stabilizes nanoscale raft domains in mixed lipid bilayers. Proc. Natl. Acad. Sci. U.S.A., 110(12):4476–4481, 2013.

[54] Maikel C. Rheinstädter and Ole G. Mouritsen. Small-scale structures in fluid cholesterol-lipid bilayers. Curr. Opin. Colloid Interface Sci., 18:440–447, 2013.

[55] Maikel C. Rheinstädter Richard J. Alsop. Lipid rafts in binary lipid/cholesterol bilayers. In Angel Catalá, editor, Membrane organization and lipid rafts in the cell and artificial membranes, Cell Biology Research Progress, pages 17–42. Nova, 2016.

[56] Annarita Ciana, Cesare Achilli, and Giampaolo Minetti. Membrane rafts of the human red blood cell. Molecular membrane biology, 31(2-3):47–57, 2014.

[57] Ilya Mikhalyov and Andrey Samsonov. Lipid raft detecting in membranes of live erythrocytes. Biochimica et Biophysica Acta (BBA)-Biomembranes, 1808(7):1930–1939, 2011.

[58] Werner A. Müller, Stephan Frings, and Frank Möhrlen. Tier- und Humanphysiologie, page 156f. Springer Berlin Heidelberg, 2015. ISBN 978-3-662-43942-5.

[59] sigmaaldrich.com. Blood basics. `http://www.sigmaaldrich.com/life-science/metabolomics/enzyme-explorer/learning-center/plasma-blood-protein/blood-basics.html`, 2017. [Online; accessed 08-April-2017].

[60] Mary Louise Turgeon. Clinical Hematology: Theory and Procedures. Lippincott Williams & Wilkins, Baltimore, 2012. ISBN 978-1608310760.

[61] C. E. McLaren, G. M. Brittenham, and V. Hasselblad. Statistical and graphical evaluation of erythrocyte volume distributions. American Journal of Physiology - Heart and Circulatory Physiology, 252(4):H857–H866, 1987.

[62] Werner A. Müller, Stephan Frings, and Frank Möhrlen. Tier- und Humanphysiologie, page 173ff. Springer Berlin Heidelberg, 2015. ISBN 978-3-662-43942-5.

[63] W. M. Tilton, C. Seaman, D. Carriero, and S. Piomelli. Regulation of glycolysis in the erythrocyte: role of the lactate/pyruvate and NAD/NADH ratios. J. Lab. Clin. Med., 118(2):146–152, Aug 1991.

[64] U. K. LAEMMLI. Cleavage of structural proteins during the assembly of the head of bacteriophage t4. Nature, 227(5259):680–685, aug 1970.

[65] Gerald Karp. Molekulare Zellbiologie (Springer-Lehrbuch) (German Edition), page 939. Springer Berlin Heidelberg, 2005. ISBN 3-540-23857-3.

[66] Wikipedia. Polyacrylamide gel electrophoresis — Wikipedia, the free encyclopedia. `http://en.wikipedia.org/w/index.php?title=Polyacrylamide%20gel%20electrophoresis&oldid=781702671`, 2017. [Online; accessed 26-May-2017].

[67] Gerald Karp. Molekulare Zellbiologie (Springer-Lehrbuch) (German Edition), page 186ff. Springer Berlin Heidelberg, 2005. ISBN 3-540-23857-3.

[68] Narla Mohandas and Patrick G Gallagher. Red cell membrane: past, present, and future. Blood, 112(10):3939–3948, 2008.

[69] Theodore L Steck. The organization of proteins in the human red blood cell membrane a review. The Journal of cell biology, 62(1):1–19, 1974.

[70] E. Hempelmann and O. Götze. Characterization of membrane proteins by polychromatic silver staining. Hoppe Seyler's Z Physiol Chem, 368:241–242, 1984.

[71] W. B. Gratzer. The red cell membrane and its cytoskeleton. Biochemical Journal, 198(1):1–8, 1981.

[72] M Lucio, JLFC Lima, and S Reis. Drug-membrane interactions: significance for medicinal chemistry. Current medicinal chemistry, 17(17):1795–1809, 2010.

[73] Lenard M Lichtenberger, Yong Zhou, Vasanthi Jayaraman, Janice R Doyen, Roger G O'Neil, Elizabeth J Dial, David E Volk, David G Gorenstein, Mohan Babu Boggara, and Ramanan Krishnamoorti. Insight into nsaid-induced membrane alterations, pathogenesis and therapeutics: characterization of interaction of nsaids with phosphatidylcholine. BBA-MOL CELL BIOL L, 1821 (7):994–1002, 2012.

[74] Gerald J Roth, Nancy Stanford, and Philip W Majerus. Acetylation of prostaglandin synthase by aspirin. Proc. Natl. Acad. Sci. U.S.A., 72(8):3073–3076, 1975.

[75] Carlo Patrono, Luis A García Rodríguez, Raffaele Landolfi, and Colin Baigent. Low-dose aspirin for the prevention of atherothrombosis. N. Engl. J. Med., 353(22):2373–2383, 2005.

[76] Mario Suwalsky, Jessica Belmar, Fernando Villena, María José Gallardo, Malgorzata Jemiola-Rzeminska, and Kazimierz Strzalka. Acetylsalicylic acid (aspirin) and salicylic acid interaction with the human erythrocyte membrane bilayer induce in vitro changes in the morphology of erythrocytes. Archives of biochemistry and biophysics, 539(1):9–19, 2013.

[77] Yong Zhou, Kwang-Jin Cho, Sarah J Plowman, and John F Hancock. Nonsteroidal anti-inflammatory drugs alter the spatiotemporal organization of ras proteins on the plasma membrane. Journal of Biological Chemistry, 287(20): 16586–16595, 2012.

[78] John Katsaras. Adsorbed to a rigid substrate, dimyristoylphosphatidylcholine multibilayers attain full hydration in all mesophases. Biophysical Journal, 75: 2157–2162, 1998.

[79] E Beutler, C West, and KG Blume. The removal of leukocytes and platelets from whole blood. J Lab Clin Med, 88(2):328–333, 1976.

[80] Giampaolo Minetti, Stephane Egée, Daniel Mörsdorf, Patrick Steffen, Asya Makhro, Cesare Achilli, Annarita Ciana, Jue Wang, Guillaume Bouyer, Ingolf Bernhardt, Christian Wagner, Serge Thomas, Anna Bogdanova, and Lars Kaestner. Red cell investigations: Art and artefacts. Blood Reviews, 27(2): 91 – 101, 2013. ISSN 0268-960X.

[81] D. Tortorella and E. London. Method for efficient pelleting of small unilamellar model membrane vesicles. Analytical Biochemistry, 217(2):176 – 180, 1994. ISSN 0003-2697.

[82] R. Richter, A. Mukhopadhyay, and A. Brisson. Pathways of lipid vesicle deposition on solid surfaces: A combined QCM-D and AFM study. Biophys. J., 85:3035–3047, 2003.

[83] Clare L. Armstrong, Martin D. Kaye, Michaela Zamponi, Eugene Mamontov, Madhusudan Tyagi, Timothy Jenkins, and Maikel C. Rheinstädter. Diffusion in single solid supported lipid bilayers studied by quasi-elastic neutron scattering. Soft Matter, 6:5864–5867, 2010.

[84] M. Lúcio, C. Nunes, D. Gaspar, K. Golebska, M. Wisniewski, J.L.F.C. Lima, G. Brezesinski, and S. Reis. Effect of anti-inflammatory drugs in phosphatidylcholine membranes: A fluorescence and calorimetric study. Chemical Physics Letters, 471(4-6):300 – 309, 2009.

[85] H. Dies, L. Toppozini, and M.C. Rheinstädter. The interaction between amyloid-β peptides and anionic lipid membranes containing cholesterol and

melatonin. PLOS ONE, pages 1–17, 2014. doi: 10.1371/journal.pone.0099124.

[86] J. Katsaras, V. A. Raghunathan, E. J. Dufourc, and J. Dufourcq. Evidence for a two-dimensional molecular lattice in subgel phase dppc bilayers. Biochemistry, 34(14):4684–4688, 1995.

[87] T.T. Mills, J. Huang, G.W. Feigenson, and J.F. Nagle. Effects of cholesterol and unsaturated dopc lipid on chain packing of saturated gel-phase dppc bilayers. Gen. Physiol. Biophys., 28:126–139, 2009.

[88] Richard J Alsop, Adree Khondker, Jochen S Hub, and Maikel C Rheinstädter. The lipid bilayer provides a site for cortisone crystallization at high cortisone concentrations. Scientific reports, 6:1–10, 2016.

[89] Nicole Pinto, Fei-Chi Yang, Atsuko Negishi, Maikel C. Rheinstädter, Todd E. Gillis, and Douglas S. Fudge. Self-assembly enhances the strength of fibers made from vimentin intermediate filament proteins. Biomacromolecules, 15 (2):574–581, 2014.

[90] Fei-Chi Yang, Robert D. Peters, Hannah Dies, and Maikel C. Rheinstädter. Hierarchical, self-similar structure in native squid pen. Soft Matter, 10:5541–5549, 2014.

[91] Fei-Chi Yang, Yuchen Zhang, and Maikel C Rheinstädter. The structure of people's hair. PeerJ, 2:e619, 2014.

[92] Yuchen Zhang, Richard J Alsop, Asfia Soomro, Fei-Chi Yang, and Maikel C Rheinstädter. Effect of shampoo, conditioner and permanent waving on the molecular structure of human hair. PeerJ, 3:e1296, 2015.

[93] Sébastien Neukirch, Alain Goriely, and Andrew C Hausrath. Chirality of coiled coils: elasticity matters. Physical review letters, 100(3):038105, 2008.

[94] FHC Crick. Is α-keratin a coiled coil? Nature, 170:882 – 883, 1952.

[95] C Cohen and DA Parry. α-helical coiled coils: more facts and better predictions. Science, 263(5146):488–489, 1994. doi: 10.1126/science.8290957.

[96] Andrei N Lupas and Markus Gruber. The structure of α-helical coiled coils. Advances in protein chemistry, 70:37–38, 2005.

[97] T.H. Watts, A.A. Brian, J.W. Kappler, P. Marrack, and H.M. McConnell. Antigen presentation by supported planar membranes containing affinity-purified I-A^d. Proc. Natl. Acad. Sci. U.S.A., 81:7564–7568, 1984.

[98] Ilya Reviakine and Alain Brisson. Formation of supported phospholipid bilayers from unilamellar vesicles investigated by atomic force microscopy. Langmuir, 16(4):1806–1815, 2000. ISSN 0743-7463. doi: 10.1021/la9903043.

[99] John F. Nagle and Stephanie Tristram-Nagle. Structure of lipid bilayers. Biochim. Biophys. Acta, 1469:159–195, 2000.

[100] S.H. Chen, C.Y. Liao, H.W. Huang, T.M. Weiss, M.C. Bellisent-Funel, and F. Sette. Collective dynamics in fully hydrated phospholipid bilayers studied by inelastic x-ray scattering. Phys. Rev. Lett., 86:740–743, 2001.

[101] M. C. Rheinstädter, C. Ollinger, G. Fragneto, F. Demmel, and T. Salditt. Collective dynamics of lipid membranes studied by inelastic neutron scattering. Phys. Rev. Lett., 93:108107, 2004.

[102] M. Tanaka and E. Sackmann. Polymer-supported membranes as models of the cell surface. Nature, 437:656–663, 2005.

[103] Maikel C. Rheinstädter, Wolfgang Häussler, and Tim Salditt. Dispersion relation of lipid membrane shape fluctuations by neutron spin-echo spectrometry. Phys. Rev. Lett., 97:048103, 2006.

[104] Xinjian Zhou, Jose M Moran-Mirabal, Harold G Craighead, and Paul L McEuen. Supported lipid bilayer/carbon nanotube hybrids. Nature nanotechnology, 2(3):185–190, 2007.

[105] Norbert Kučerka, Mu-Ping Nieh, and John Katsaras. Fluid phase lipid areas and bilayer thicknesses of commonly used phosphatidylcholines as a function of temperature. Biochimica et Biophysica Acta (BBA) - Biomembranes, 1808 (11):2761 – 2771, 2011.

[106] Bradley Moores, Elizabeth Drolle, Simon J Attwood, Janet Simons, and Zoya Leonenko. Effect of surfaces on amyloid fibril formation. PLoS One, 6(10): e25954, 2011.

[107] Maikel Rheinstädter, Laura Toppozini, and Hannah Dies. The interaction of bio-molecules with lipid membranes studied by x-ray diffraction. Zeitschrift für Physikalische Chemie, 228(10-12):1105–1120, 2014.

[108] Drew Marquardt, Richard J Alsop, Maikel C Rheinstädter, and Thad A Harroun. Neutron scattering at the intersection of heart health science and biophysics. Journal of Cardiovascular Development and Disease, 2(2):125–140, 2015.

[109] Kelly Cathcart, Amit Patel, Hannah Dies, Maikel C Rheinstädter, and Cécile Fradin. Effect of cholesterol on the structure of a five-component mitochondria-like phospholipid membrane. Membranes, 5(4):664–684, 2015.

[110] J Yang, L K Tamm, T W Tillack, and Z Shao. New approach for atomic force microscopy of membrane proteins. the imaging of cholera toxin. Journal of molecular biology, 229(2):286–90, jan 1993. ISSN 0022-2836. doi: 10.1006/jmbi.1993.1033.

[111] S A Jewell, R W Titball, J Huyet, C E Naylor, A K Basak, P Gologan, C P Winlove, and P G Petrov. Clostridium perfringensα-toxin interaction with red cells and model membranes. Soft matter, 11(39):7748–61, 2015. ISSN 1744-6848. doi: 10.1039/c5sm00876j.

[112] S Knutton, JB Finean, R Coleman, and AR Limbrick. Low-angle x-ray diffraction and electron-microscope studies of isolated erythrocyte membranes. Journal of cell science, 7(2):357–371, 1970.

[113] James B Stamatoff, Samuel Krimm, and Nancy Reid Harvie. X-ray diffraction studies of human erythrocyte membrane structure. Proceedings of the National Academy of Sciences, 72(2):531–534, 1975.

[114] Travis Harrison, Benjamin U Samuel, Thomas Akompong, Heidi Hamm, Narla Mohandas, Jon W Lomasney, and Kasturi Haldar. Erythrocyte g protein-coupled receptor signaling in malarial infection. Science, 301(5640):1734–1736, 2003.

Eidesstattliche Versicherung

Hiermit versichere ich an Eides statt, dass ich die vorliegende Arbeit selbstständig und ohne Benutzung anderer als der angegebenen Hilfsmittel angefertigt habe. Die aus anderen Quellen oder indirekt übernommenen Daten und Konzepte sind unter Angabe der Quelle gekennzeichnet. Die Arbeit wurde bisher weder im In- noch im Ausland in gleicher oder ähnlicher Form in einem Verfahren zur Erlangung eines akademischen Grades vorgelegt.

Saarbrücken, den 29. Mai 2017 Sebastian Himbert

Acknowledgments

I had a great deal of support in the past years and for this tremendous help, I would like to give thanks.
Most importantly I would like to thank my supervisors Dr. Christian Wagner and Dr. Maikel Rheinstädter for giving me the opportunity to spent an incredible year at the McMaster University in Canada. To Maikel, thank you and your whole family for welcoming me in Canada. Your contagious enthusiasm, your patience and flexibility made it easy to get excited about this and all other projects, I worked on. Further, I would like to thank Rick Alsop for the great support and help, he gave me over the entire year. Thank you for proofreading this thesis and thank you for all the fun we had. I would also like to thank all undergraduate students in Maikel's group, especially Mindy Chapman, Adree Khondker and Alexander Dhaliwal who helped in various projects.
To Christian, thank you for your support, guidance and mentorship over the past years. The work in your group as undergraduate, as well as graduate student has always been fun, interesting, fruitful and formed me as scientist. I would also like to acknowledge all group members, especially Alexander Kihm for proofreading this thesis. Special thanks to Karin Kretsch for your support in the lab and to Elke Huschens for always being there to help me with any administrative problems, I struggled with.
My sincere thanks goes to all collaborators. This thesis wouldn't have been possible without their help, expertise and enthusiasm: Dr. David Deamer, Dr. Jose Moran Mirabal, Dr. Dawn Bowdish, Dr. Chris Vershoor and Dr. Lars Kaestner. I would also thank their students: Laura Hertz and Markus Rose. Special thanks to Dessi Loukov for taking my blood without any pain.

Finally I would like to acknowledge the support of my familiy and friends over the years. Especially, I would like to thank my parents Susanne and Stefan Himbert and my sister Caroline Himbert. They helped me through all the good and bad times and helped to shape me as a person. To my friends Jan, Erik, Rebecca, Friederike, Marco and Yolanda, thank you for what you do best, being amazing friends!